Appendix A:

Experimental Methods and Supplementary Figures for Chapter II: Singlet Fission in HDPP-Pent, $Li_2(DPP\text{-}Pent)_2$, and KDPP-Pent

Methods

Rotating Frame Nuclear Overhauser Spectroscopy

ROESY, like standard nuclear Overhauser enhancement spectroscopy (NOESY), probes through-space dipolar couplings between nuclear spins. NOESY effectively operates by saturating the transition of a particular nuclear spin and observing changes in intensity of the rest of the spectrum. As the saturated spin undergoes relaxation toward thermal equilibrium, dipolar interactions with another nearby nuclear spin can give rise to relaxation pathways that perturb the population distribution of this second unsaturated spin system, leading to a change in signal intensity for this other transition. Two major pathways for this perturbation exist: zero-quantum and double-quantum transitions. In a magnetic field, the nuclear Zeeman states are split with α spin states lower in energy than the β states. Zero-quantum transitions ($\alpha_I\beta_S \leftrightarrow \beta_I\alpha_S$), or flip-flop transitions, preserve the total M_I of the two-spin system but exchange the individual spin states of spins I and S. Double-quantum transitions, on the other hand, change the total M_I by ±2 ($\alpha_I\alpha_S \leftrightarrow \beta_I\beta_S$).

If we saturate spin S, we will overpopulate the higher energy β_S state and relaxation will favor transitions that lead from β_S to α_S to restore the equilibrium populations. We can see that zero-quantum transitions $\alpha_I\beta_S \rightarrow \beta_I\alpha_S$, will lead to a simultaneous increase in the β_I population, which decreases the population difference between α_I and β_I, leading to a decrease in absorption intensity for spin I. For double-quantum transitions $\beta_I\beta_S \rightarrow \alpha_I\alpha_S$, the population difference between α_I and β_I will on average increase, leading to an increase in the absorption signal intensity for spin I. This leads to two different relaxation mechanisms that will impact the sign of the observed change in signal intensity.

These transitions require exchange of energy between the spin system and the environment. For the zero-quantum transition, the energy required is proportional only to the difference in transition frequency for the two spins I and S, whereas for double-quantum transitions, it is proportional to the sum of the transition frequencies. As a result, double quantum transitions require greater energetic exchange with the environment. The zero- and double-quantum transitions may couple to molecular motions on the frequency scale of the transitions. In this case, rotational motion from molecular tumbling in solution gives rise to the appropriate spectral density function covering these transitions. Because double-quantum transitions require greater energy, higher frequency rotational motion is required for this relaxation pathway to be efficient. As a result, the double-quantum transition is dominant in small molecules with fast rotational tumbling, leading to positive NOE signals. As the average molecular size increases, the rotational motion slows and the double-quantum transition becomes inefficient, allowing the zero-quantum transition to dominate NOE relaxation in large molecules, such as proteins, which gives negative NOE signals.

This trend necessarily means that there is an intermediate regime for molecular size in which the double- and zero-quantum transitions are equally efficient, giving rise to a null NOE signal intensity. As the size (taken as a sphere) and molecular weight can be connected via the Stokes-Einstein equation, the molecular weight for this null region is typically given around 1 kDa. The DPP-Pent subunit stands at molecular weight of 1124, and as a result, we were unable to resolve NOE cross-correlation signals even for through-space interactions that should be inherent to the pentacene moiety (i.e. H_aH_b).

These same relaxation pathways are present in ROESY experiments. However, ROESY differs from NOESY in the pulse sequency. In NOESY, spin mixing is allowed to occur while polarized along the z-axis of the laboratory frame (along the external magnetic field where α and β are reasonable eigenstates). In ROESY, after the initial $\pi/2$ pulse, an effectively continuous-wave RF pulse is applied along the direction of the magnetization in the transverse plane, which effectively holds the magnetization in the XY plane, a process known as spin-locking. The spin mixing now occurs between dressed states of the system that are quantized against the B_1 field of the RF spin-locking pulse. This B_1 field is significantly weaker in magnitude than the external magnetic field B_0, and as a result the transition frequencies between the dressed states are significantly reduced. The result of this is that the double-quantum transition is effectively always operative and dominant even for large molecules, and the ROE signal intensity is always positive with respect to molecular weight/size. This has the advantage of allowing resolution of the NOE signal even when NOESY pulse sequences provide a null cross-correlation intensity. ROESY was therefore utilized for $Li_2(DPP\text{-}Pent)_2$ and KDPP-Pent in this study.

Steady-State Emission Spectroscopy

Corrected room temperature emission spectra were collected in the Beckman Institute Laser Resource Center using a modified Jobin Yvon Spec Fluorolog-3 instrument. Samples were excited with a xenon arc lamp, employing a monochromator for wavelength selection, and emission was detected at 90° using two Ocean Optics EQDPro CCD spectrometers spanning 300 to 930 nm.

Fluorescence quantum yields were determined via the comparative method in which the experimental quantum yields were measured relative to a known standard under the same excitation conditions. Rhodamine-6G in EtOH was used as a standard ($\Phi_S = 0.95$). All samples were diluted such that the maximum absorbance values were less than 0.1. Pentacene samples of unknown quantum yield were prepared in toluene and added to 1 cm glass emission cuvettes and sealed with a Kontes plug under $N_{2(g)}$ atmosphere. Samples were excited at λ_{ex} = 530 nm. The unknown quantum yields (Φ_X) were calculated with Equation 1 using the absorbance values $A(\lambda_{ex})$, the integrated fluorescence intensities $F(\lambda_{ex})$, and correcting for the differing indices of refraction between EtOH and toluene.

$$\Phi_X = \frac{A_S(\lambda_{ex})}{A_X(\lambda_{ex})} \cdot \frac{F_X(\lambda_{ex})}{F_S(\lambda_{ex})} \cdot \frac{n_X^2}{n_S^2} \cdot \Phi_S \qquad Eq\ (1)$$

Time-Resolved Luminescence Spectroscopy

The 1064 nm output of a Nd:YAG laser (Spectra Physics Vanguard) was regeneratively amplified (Continuum) and frequency doubled using a potassium dihydrogen phosphate (KDP) crystal to 532 nm excitation pulses (~10 ps, 10 Hz). Luminescence was collected 90° from the excitation, passed through a polarizer oriented at the magic angle, then directed onto the entrance slit of a monochromator for wavelength selection. Detection was achieved using a streak camera (Hamamatsu C5680) in photon-counting mode, and data were collected over a 50 ns time window. Samples were prepared in sealed 1 cm quartz cuvettes under $N_{2(g)}$ and were stirred during data acquisition.

Transient Absorption Spectroscopy

The 800 nm output of a 5 W, 1 kHz pulsed Ti:sapphire amplifier (Coherent Astrella) was partitioned with a 50:50 beamsplitter. One half was fed into an OPerA Solo optical parametric amplifier tuned to 550 nm output, which was used as the excitation pump and routed through a chopper and into a joint femtosecond and nanosecond HELIOS FIRE / EOS transient absorption (TA) spectrometer (Ultrafast Systems). For femtosecond experiments, a small portion of the other half of the Ti:sapphire output was routed into the spectrometer and used to generate broadband probe light of the appropriate wavelength region (visible or near-infrared). For nanosecond experiments, a separate white light fiber laser was employed as the probe light. Samples were prepared in sealed 2 mm glass cuvettes under $N_{2(g)}$ and were stirred during data acquisition. Data were processed using Ultrafast Systems Surface Xplorer software for chirp and time zero corrections. The rest of the data workup was performed in MATLAB. For fsTA datasets, pre-time zero spectral vectors were averaged and subtracted from the rest of the dataset to remove background pump scatter. Pre-time zero spectral vectors were similarly averaged in the nsTA datasets and then subtracted up to 20 μs delay times as pump scatter is not detected beyond this threshold by the EOS.

I. Experimental Considerations

General Information

Air- and moisture-sensitive compounds were handled with standard Schlenk line techniques or in a $N_{2(g)}$ atmosphere glove box. When air- and moisture-free techniques were required, dry solvents were acquired from an alumina solvent still. No unexpected or unusually high safety hazards were encountered. 2,6-dibromopyridine was purchased from Combi-Blocks Inc. and used without further purification. Tin (II) dichloride dihydrate was purchased from Matrix Scientific and used without further purification. $Pd(PPh_3)_4$ was purchased from Oakwood Chemicals, stored under inert atmosphere, and used without further purification. Lithium hexamethyldisilazide and potassium hexamethyl disilazide were purchased from Sigma Aldrich, stored in an inert atmosphere glovebox, and used without further purification. 13-hydroxy-13-[(triisopropylsilyl)ethynyl]pentacen-6(13H)-one (Ketone 1, Figure S1)[1] and 2,5-bis(pinacolatoboranyl)pyrrole[2] were synthesized according to previous reports. ^1H, ^{13}C, and 2D NMR spectra were collected on a 400 MHz Varian spectrometer. All pentacene solution-state samples for optical spectroscopy were prepared in an inert-atmosphere glovebox using solvents dried and purified on an alumina drying column and degassed prior to being brought into the glovebox. Steady-state absorption spectra were collected using a Varian Cary 500 Scan spectrophotometer. Glotaran (http://glotaran.org), a user interface for the R-based time-resolved fitting software TIMP, was used for kinetic modeling of the transient absorption data.[3]

II. Synthetic Procedures

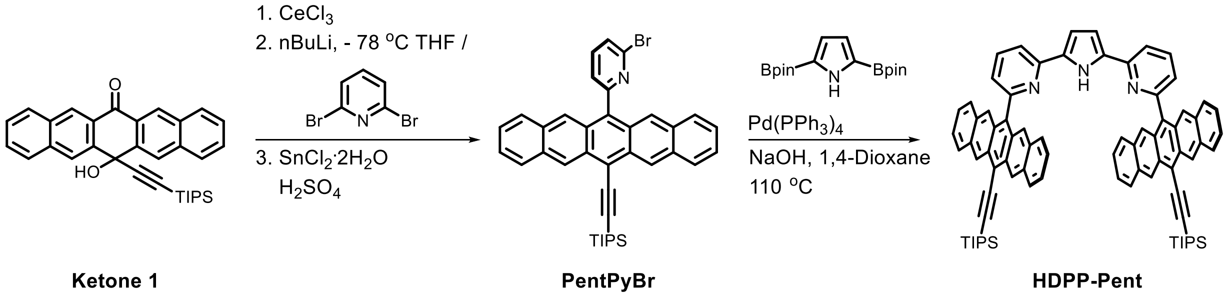

Figure A.1 Synthetic scheme for HDPP-Pent. Ketone 1 is activated with $CeCl_3$ then converted into PentPyBr by deprotonation and nucleophilic attack by monolithiated 2,6-dibromopyridine at -78 °C, followed by reductive aromatization with $SnCl_2·2H_2O$. HDPP-Pent is then furnished after a double-Suzuki-Miyaura coupling of PentPyBr with 2,5-bis(pinacolatoboranyl)pyrrole using catalytic $Pd(PPh_3)_4$.

Synthesis of PentPyBr

Ketone 1 (10 mmol) was dissolved in THF in an oven-dried flask under inert conditions. $CeCl_3$ (20 mmol) was added under positive $N_{2(g)}$ pressure and the mixture was stirred for 1 h at room temperature. In a separate flask under nitrogen atmosphere, dibromopyridine (30 mmol) was dissolved in THF and cooled to -78 °C. nBuLi (1.6M solution in hexanes, 30 mmol) was then added slowly to the pyridine solution, which was stirred for 30 min to achieve monolithiation. The solution of Ketone 1 was cooled to -78 °C and the lithiated pyridine solution was slowly cannula transferred under positive nitrogen pressure with stirring. The mixture was warmed to room temperature and stirred for 15 h. Aqueous ammonium chloride solution was slowly added to quench. The brown solution was filtered through a pad of celite to remove salts. The organics were taken up in dichloromethane and washed with brine (2x), dried over Mg_2SO_4, and concentrated to an oily solid. This material was taken up in THF (80 mL) and transferred to a three-neck roundbottom flask. The solution was sparged with $N_{2(g)}$ and $SnCl_2·2H_2O$ (20 mmol) was added followed by slow addition of 10% H_2SO_4 (3 mL). The solution was sparged again and stirred for 3 h under nitrogen atmosphere at room temperature. The reaction was neutralized with $K_2CO_{3(aq)}$ and the reaction mixture was filtered through celite. The product was extracted with dichloromethane and dried over Mg_2SO_4. The mixture was concentrated, and the target compound was crashed from methanol to give a dark blue powder. ^{1}H NMR (400 MHz, $CDCl_3$, 25 ºC): δ 9.37 (s, 2H), 8.16 (s, 2H), 7.96 (d, *J* = 8.5 Hz, 2H), 7.93 – 7.89 (m, 1H), 7.81 (dd, *J* = 8.0, 1.0 Hz, 1H), 7.77 (d, *J* = 8.5 Hz, 2H), 7.60 (dd, *J* = 7.4, 1.0 Hz, 1H), 7.40 – 7.29 (m, 5H), 1.39 (s, 21H). ^{13}C NMR (101 MHz, $CDCl_3$, 25 ºC): δ 159.7, 142.7, 139.0, 134.0, 132.0, 130.9, 128.8, 128.7, 128.3, 127.5, 126.5, 126.2, 126.1, 125.9, 125.1, 119.2, 106.4, 104.7, 19.2, 11.8. HRMS (FAB+) Calcd. For $C_{38}H_{36}NSiBr$: 615.1780. Found: 615.1770.

Synthesis of HDPP-Pent

PentPyBr (2.5 g), 2,5-bis(pinacolatoboranyl)pyrrole (0.65 mg), and NaOH (8.7 mg) were added to an oven-dried Schlenk flask under nitrogen atmosphere and a degassed 9:1 1,4-dioxane/H_2O solution (100 mL) was added. $Pd(PPh_3)_4$ (5 mol%) was added under a counter-flow of $N_{2(g)}$ and the reaction mixture was heated to 110 °C for 5 h. Volatiles were removed under vacuum pressure and the organics were taken up in dichloromethane, washed with brine (2x), dried over Mg_2SO_4, filtered, and concentrated to dryness. HDPP-Pent was obtained as a blue solid by silica-column chromatography (3 : 1 Hexanes/CH_2Cl_2, followed by 5 : 1 Hexanes/THF, then 5:1:1 Hexanes/CH_2Cl_2/Toluene with 1% MeOH). ^{1}H NMR (400 MHz, CD_2Cl_2, 25 ºC): δ 10.39 (s, 1H), 8.48 (br s, 4H), 7.64 – 7.58 (m, 5H), 7.48 (d, 5H), 7.43 (br s, 4H), 7.07 (d, 2H), 6.95 (dd, J = 6.2, 2.1 Hz, 2H), 6.84 – 6.73 (m, 9H), 1.46 (br s, 42H). ^{13}C NMR (101 MHz, CD_2Cl_2, 25 ºC): δ 158.1, 149.7, 136.0, 135.8, 133.3, 130.7, 130.0, 129.6, 127.7, 127.2, 127.0, 125.0, 124.6, 124.5, 124.0, 123.6, 117.2, 116.9, 109.3, 105.4, 103.4, 19.3, 12.0.

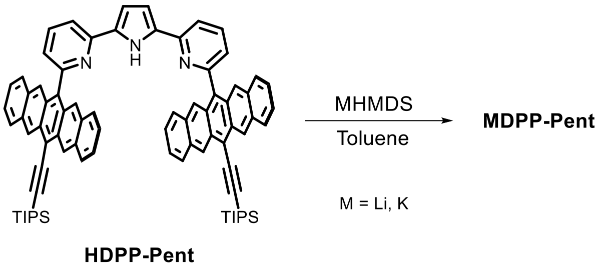

Figure A.2 Synthetic scheme for MDPP-Pent (M = Li, K). HDPP-Pent is deprotonated with the appropriate alkali metal hexamethyldisilazide (MHMDS).

Synthesis of $Li_2(DPP\text{-}Pent)_2$

HDPP-Pent (0.1 mmol) was dissolved in toluene (3 mL) and a solution of lithium hexamethyldisilazide (0.1 mmol) in toluene (2 mL) was added, and the mixture was stirred for 20 min. The solution quickly turned from blue to blue-green. Volatiles were removed via vacuum pressure and the desired product was obtained as a blue-green powder. ^{1}H NMR (400 MHz, CD_2Cl_2, 25 °C): δ 9.10 (s, 4H), δ 7.84 (d, 4H), δ 7.75 (s, 4H), δ 7.51 (d, 4H), δ 7.23 (dd, 4H), δ 6.93 (dd, 4H), δ 6.04 (m, 4H), δ 5.12 (d, 2H), δ 4.36 (s, 2H), δ 1.53 (m, 42H).

Synthesis of KDPP-Pent

HDPP-Pent (0.1 mmol) was dissolved in toluene (3 mL) and a solution of potassium hexamethyldisilazide (0.1 mmol) in toluene (2 mL) was added, and the mixture was stirred for 20 min. The solution quickly turned from blue to blue-green. Volatiles were removed via vacuum pressure and the desired product was obtained as a blue-green powder. ^{1}H NMR (400 MHz, CD_2Cl_2, 25 °C): δ 9.13 (s, 4H), δ 8.15 (s, 4H), δ 7.80 (m, 8H), δ 7.59 (d, 4H), δ 7.24 (m, 4H), δ 7.15 (m, 4H), δ 7.01 (s, 2H), δ 6.96 (d, 2H), δ 1.35 (m, 42H).

Synthesis of NaDPP-Pent

HDPP-Pent (0.1 mmol) was dissolved in toluene (3 mL) and a solution of sodium hexamethyldisilazide (0.1 mmol) in toluene (2 mL) was added, and the mixture was stirred for 20 min. The solution quickly turned from blue to blue-green. Volatiles were removed via vacuum pressure and the desired product was obtained as a blue-green powder. ^{1}H NMR (400 MHz, CD_2Cl_2, 25 °C): δ 9.07 (s, 4H), δ 8.09 (s, 4H), δ 7.79 (m, 8H), δ 7.59 (d, 4H), δ 7.24 (m, 4H), δ 7.15 (m, 4H), δ 7.04 (s, 2H), δ 6.94 (d, 2H), δ 1.36 (m, 42H).

III. 2D Rotating Frame Overhauser Effect Spectroscopy (ROESY)

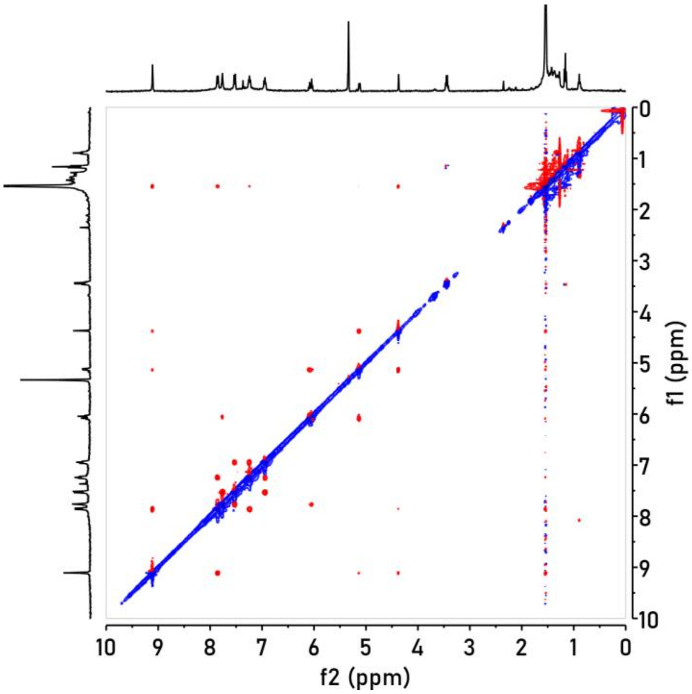

Figure A.3 2D ROESY spectrum of $Li_2(DPP\text{-}Pent)_2$ (400 MHz, CD_2Cl_2).

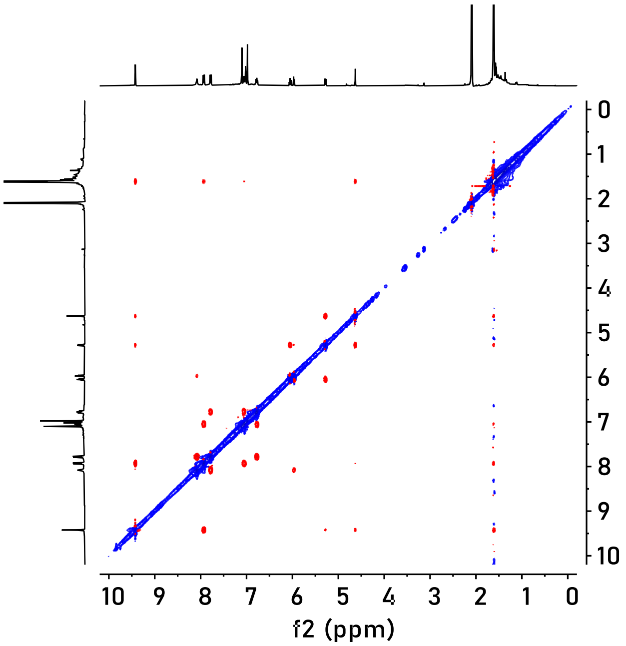

Figure A.4 2D ROESY spectrum of $Li_2(DPP\text{-}Pent)_2$ (400 MHz, toluene-d8).

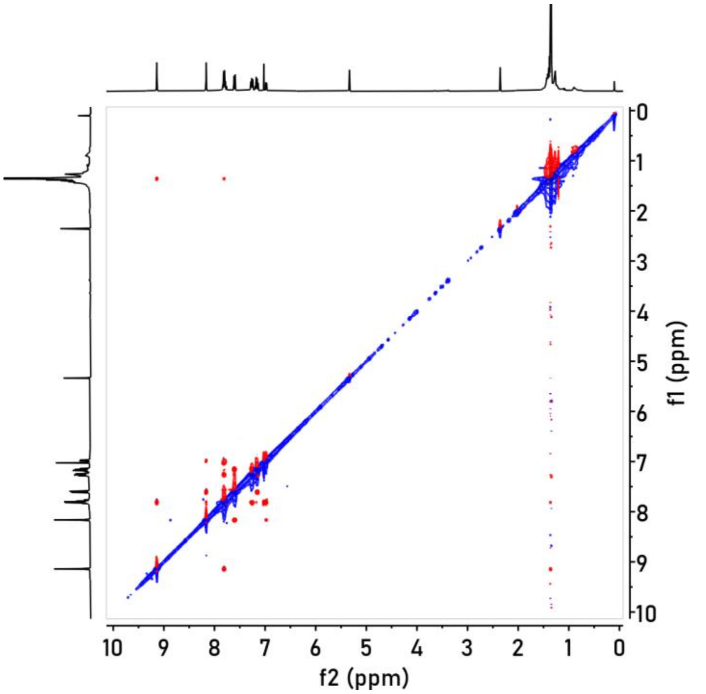

Figure A.5 2D ROESY spectrum of KDPP-Pent (400 MHz, CD_2Cl_2).

IV. Steady-State Absorption and Emission Spectroscopy

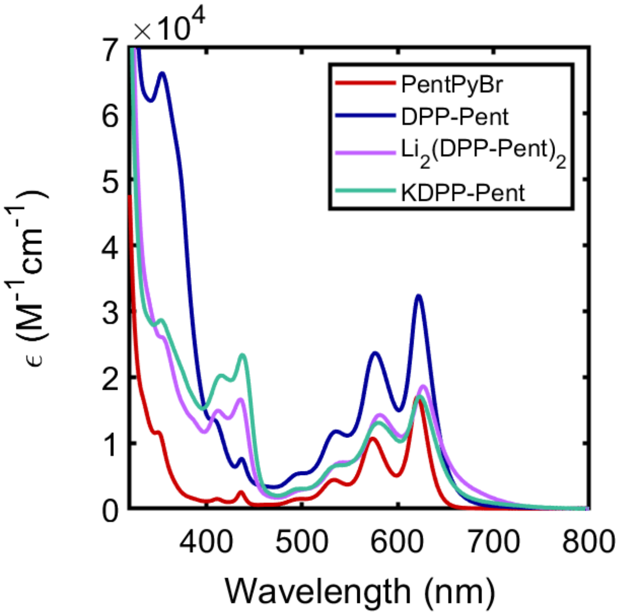

Figure A.6 Visible absorption spectra of PentPyBr (red), HDPP-Pent (blue), Li_2(DPP-Pent)$_2$ (purple), and KDPP-Pent (teal) in toluene.

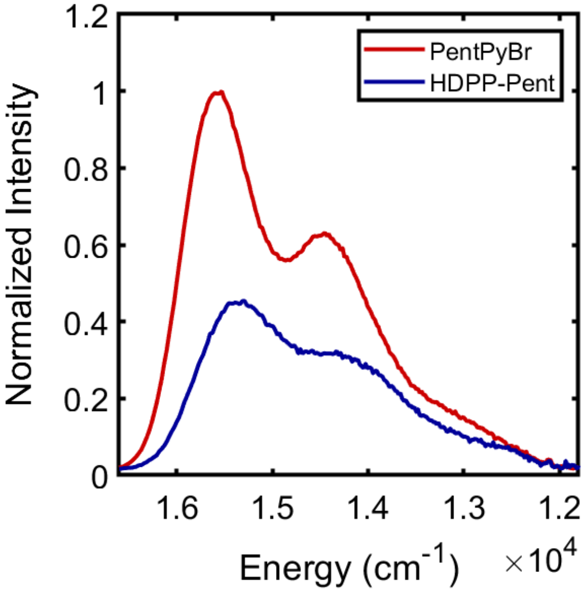

Figure A.7 Emission spectra of PentPyBr (red) and HDPP-Pent (blue). The PentPyBr maximum signal intensity was normalized to one, and the HDPP-Pent spectrum was scaled such that the integrated intensity of the samples reflected their relative estimated quantum yields.

V. Time-Resolved Luminescence Spectroscopy

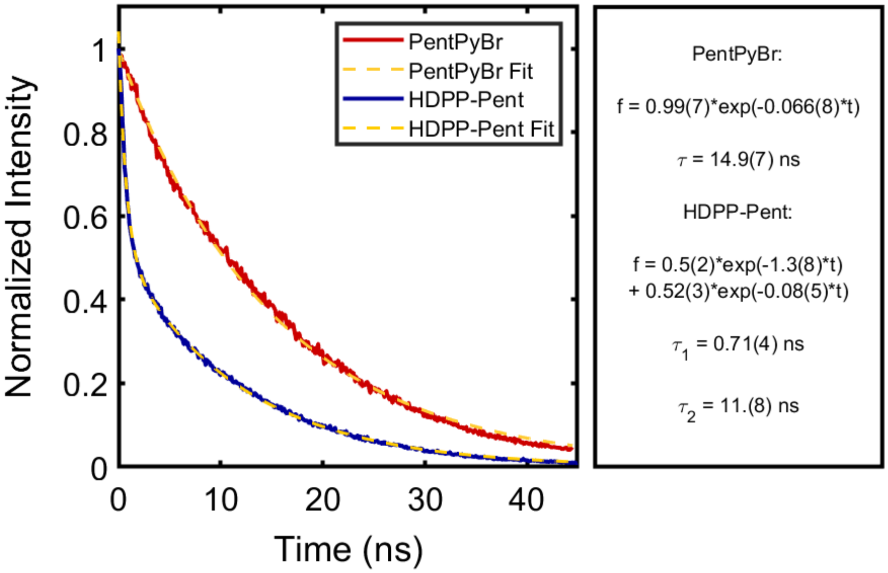

Figure A.8 Time-resolved luminescence spectra of PentPyBr (λ_{obs} = 640 nm) and HDPP-Pent (λ_{obs} = 650 nm) after excitation at 532 nm. The spectra were normalized to a maximum of 1. The fluorescence decay of PentPyBr was fit to a monoexponential function (τ = 15 ns), whereas the decay of HDPP-Pent had to be fit biexponentially (τ_1 = 0.71 ns, τ_2 = 11.8 ns).

VI. Transient Absorption Spectroscopy

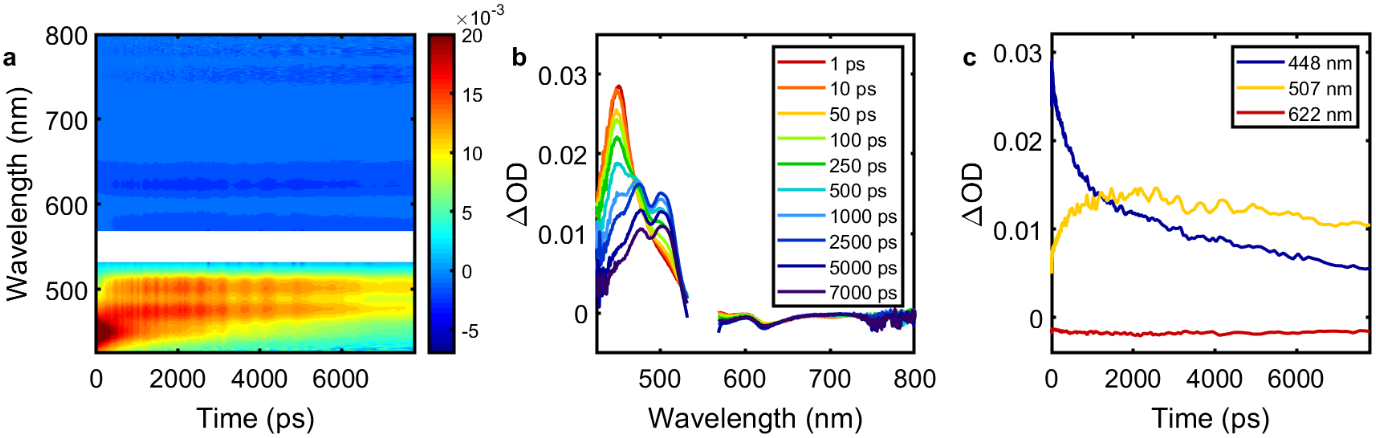

Figure A.9 Femtosecond visible transient absorption spectra of HDPP-Pent (50 µM, toluene) after excitation at 550 nm (0.100 µJ/pulse): (a) contour plot, (b) spectral traces at various time delays, (c) selected time traces at 448, 507, and 622 nm.

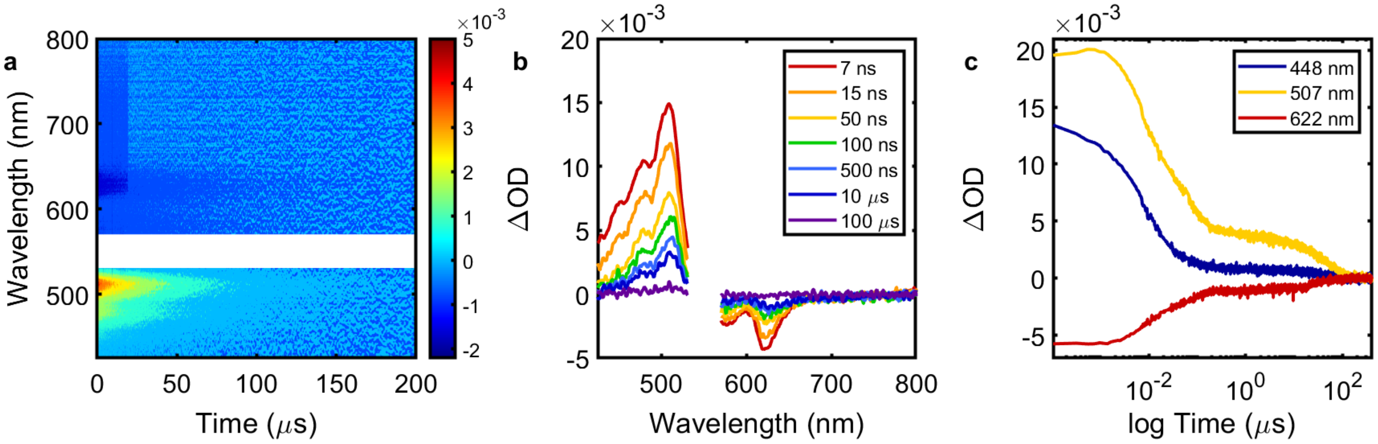

Figure A.10 Nanosecond visible transient absorption spectra of HDPP-Pent (50 µM, toluene) after excitation at 550 nm (0.100 µJ/pulse): (a) contour plot, (b) spectral traces at various time delays, (c) selected time traces at 448, 507, and 622 nm.

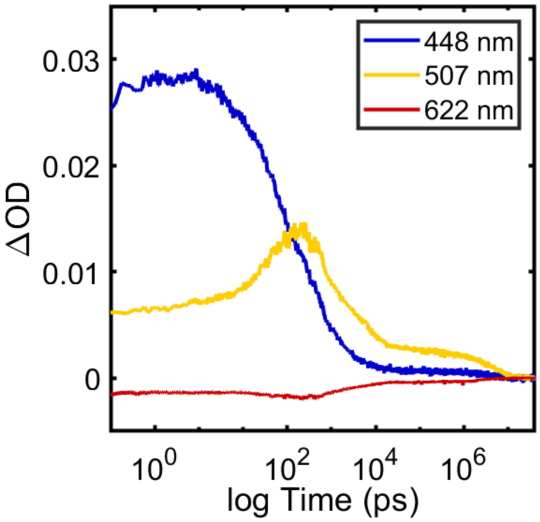

Figure A.11 Combined visible fs and ns TA spectra of HDPP-Pent (50 μM, toluene) after excitation at 550 nm (0.100 μJ/pulse); time traces selected at 448, 507, and 622 nm.

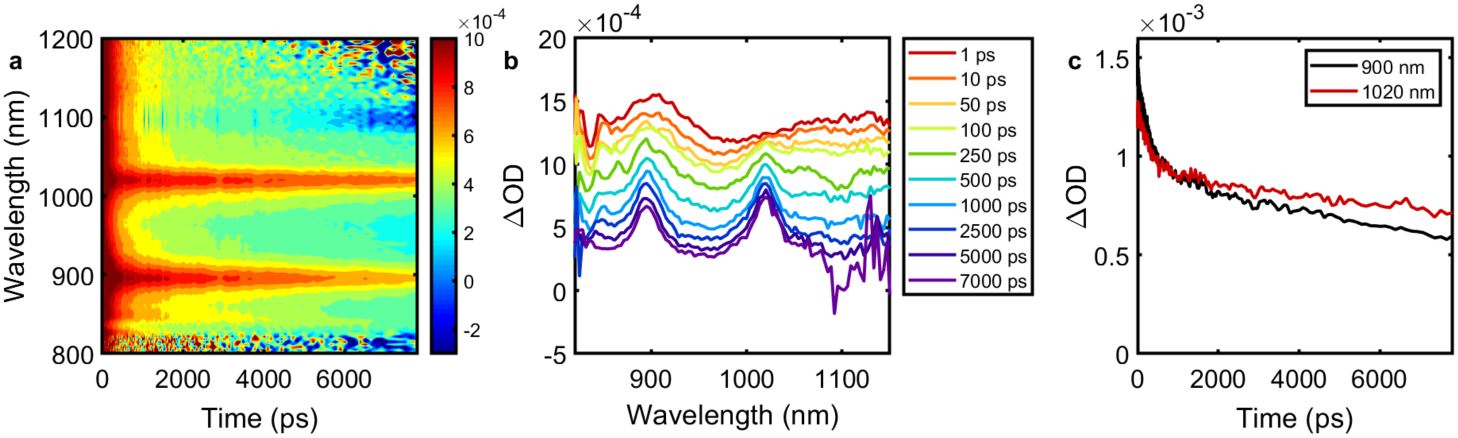

Figure A.12 Near-IR fsTA spectra of HDPP-Pent (50 µM, toluene) after excitation at 550 nm (0.100 µJ/pulse): (a) contour plot, (b) spectral traces at various time delays, (c) selected time traces at 900 and 1020 nm.

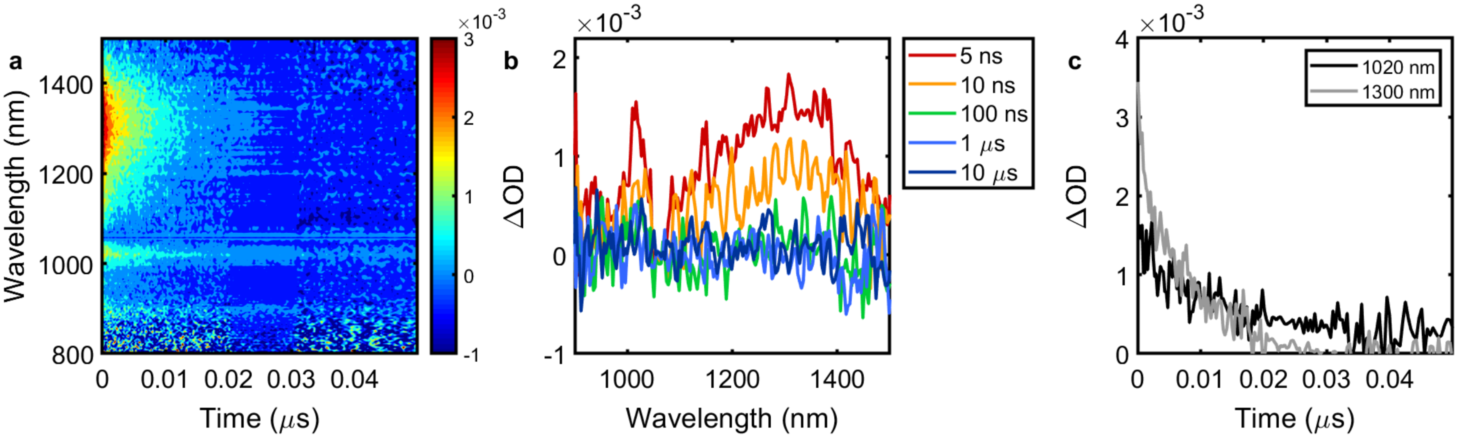

Figure A.13 Near-IR nsTA spectra of HDPP-Pent (50 μM, toluene) after excitation at 550 nm (0.100 μJ/pulse): (a) contour plot, (b) spectral traces at various time delays, (c) selected time traces at 900 and 1020 nm.

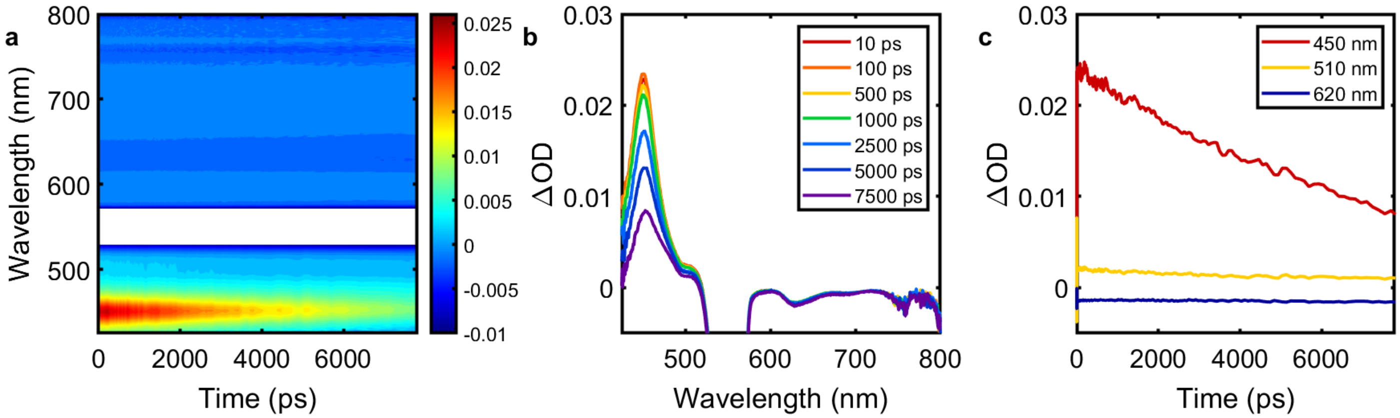

A.14 Visible fsTA spectra of PentPyBr (80 μM, toluene) after excitation at 550 nm (0.100 μJ/pulse): (a) contour plot, (b) spectral traces at various time delays, (c) selected time traces at 900 and 1020 nm.

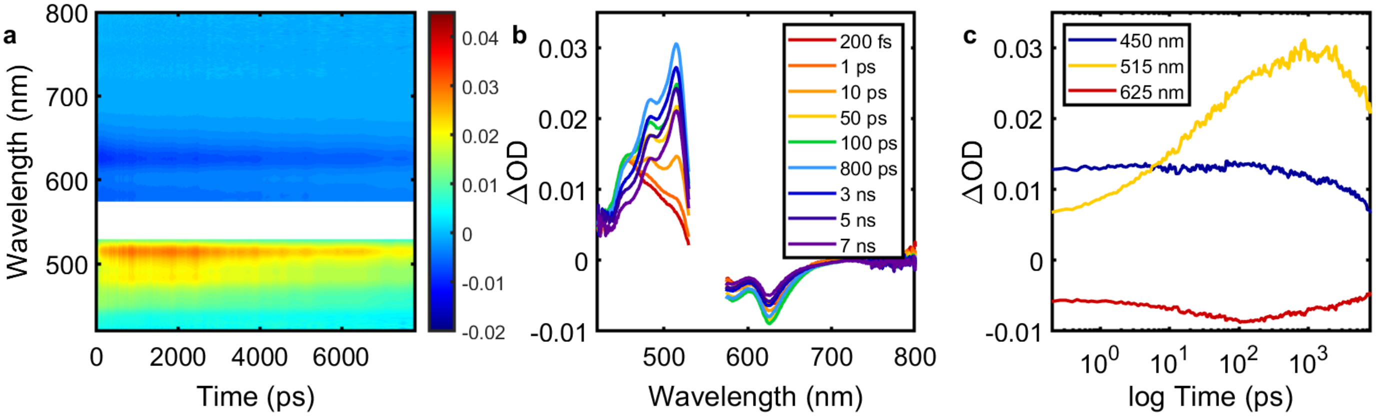

Figure A.15 Visible fsTA spectra of $Li_2(DPP\text{-}Pent)_2$ (50 μM, toluene) after excitation at 550 nm (0.100 μJ/pulse): (a) contour plot, (b) spectral traces at various time delays, (c) selected time traces at 450, 515, and 625 nm.

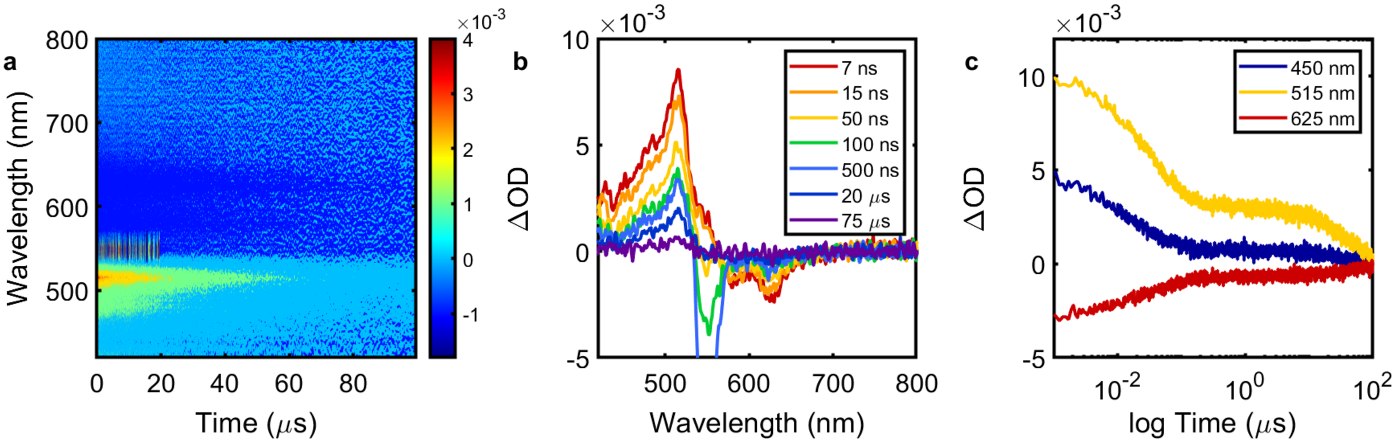

Figure A.16 Visible nsTA spectra of $Li_2(DPP\text{-}Pent)_2$ (50 μM, toluene) after excitation at 550 nm (0.100 μJ/pulse): (a) contour plot, (b) spectral traces at various time delays, (c) selected time traces at 450, 515, and 625 nm.

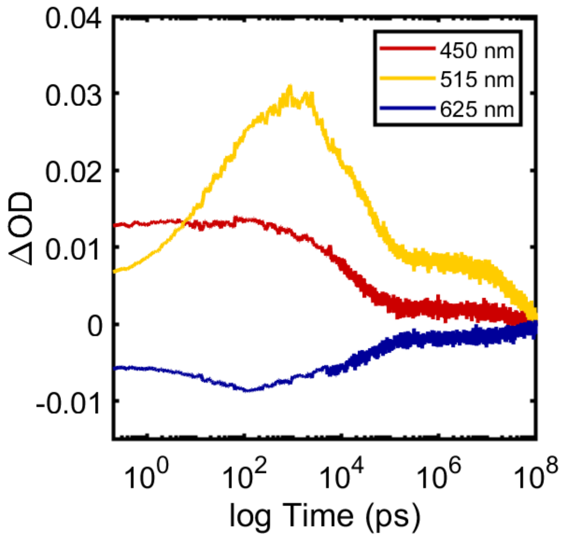

Figure A.17 Combined visible fs and ns TA spectra of Li_2(DPP-Pent)$_2$ (50 μM, toluene) after excitation at 550 nm (0.100 μJ/pulse); time traces selected at 450, 515, and 625 nm.

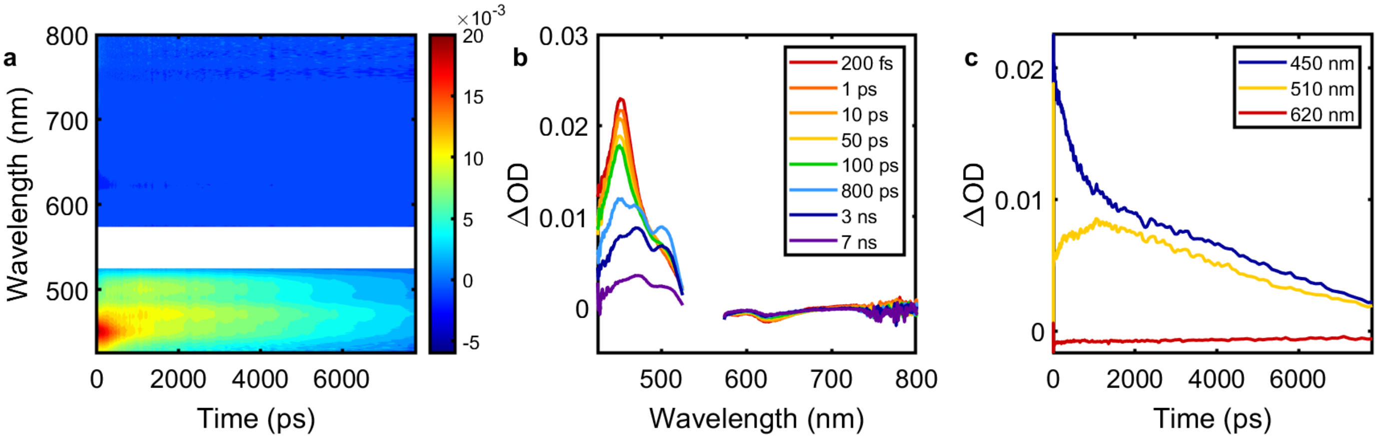

Figure A.18 Visible fsTA spectra of KDPP-Pent (50 μM, toluene) after excitation at 550 nm (0.100 μJ/pulse): (a) contour plot, (b) spectral traces at various time delays, (c) selected time traces at 450, 510, and 620 nm.

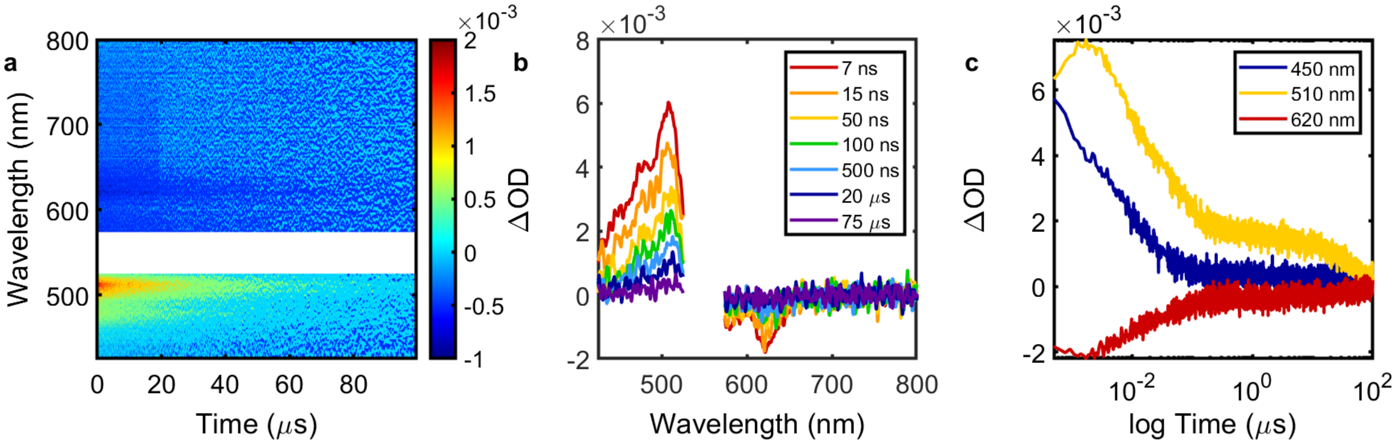

Figure A.19 Visible nsTA spectra of KDPP-Pent (50 μM, toluene) after excitation at 550 nm (0.100 μJ/pulse): (a) contour plot, (b) spectral traces at various time delays, (c) selected time traces at 450, 510, and 620 nm.

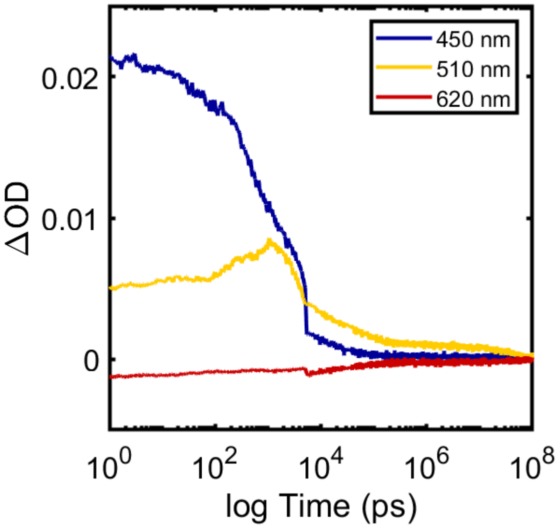

Figure A.20 Combined visible fs and ns TA spectra of KDPP-Pent (50 μM, toluene) after excitation at 550 nm (0.100 μJ/pulse); time traces selected at 450, 510, and 620 nm.

VII. Target Kinetic Analysis

HDPP-Pent

For HDPP-Pent, the time-resolved luminescence data provide information solely on the dynamics of the S_1 state independent of the TA spectroscopy. The results of the emission experiment may therefore be appropriately applied to a kinetic model for fitting the composite TA data. Our model assumes the decay of the ^{1}ESA feature should mirror the biexponential decay observed in the time-resolved emission data, as both reflect the dynamics of the S_1 state. Thus, we require terms that account for both the radiative and nonradiative relaxation pathways. Initial attempts to fit single wavelength decay curves of the ^{3}ESA feature from the nsTA data to an exponential function clearly indicated the triplet decay required at least a biexponential. In fact, attempts to model the kinetics with only a monoexponential triplet decay produced results that exhibited significant intensity of the triplet feature in the singular value decomposition (SVD) of the residual data matrix, highlighting that the monoexponential decay model does not adequately describe the decay of the ^{3}ESA feature. This is consistent with other reports of multiexponential decays in the ^{3}ESA feature reflecting geminate recombination of the triplet pair on a faster timescale than uncorrelated triplet decay.

In order to accommodate the biexponential decay of the ^{1}ESA, components 1 and 2 are set to equally reflect the ^{1}ESA spectrum and are weighted equally in initial intensity to reflect the weighting coefficients from the time-resolved fluorescence results (Supplementary Table S1). Components 3 and 4 are allowed to vary spectrally, but ultimately both reflect the ^{3}ESA feature. Component 1 decays into components 3 and 4 equally with a rate constant k_1, component 2 decays to the ground state with rate constant k_2, and components 3 and 4 decay to the ground state with rate constants k_3 and k_4 respectively.

Table A.1 HDPP-Pent visible fs and ns TA target analysis; no parameters fixed

	k (s^{-1})	Standard Error
k_1	$1.3(4) \times 10^9$	1.07×10^7
k_2	$2.0(2) \times 10^8$	2.31×10^6
k_3	$2.6(6) \times 10^7$	1.72×10^5
k_4	$2.8(1) \times 10^4$	3.32×10^2
	τ (ps)	
τ_1	$7.4(6) \times 10^2$	
τ_2	$4.9(5) \times 10^3$	
τ_3	$3.7(6) \times 10^4$	
τ_4	$3.5(6) \times 10^7$	

	1	2	3	4
1				
2		k_2		
3	k_1		k_3	
4	k_1			k_4

Fitted kinetic parameters obtained from a four-component model of the composite visible fs and ns TA data of HDPP-Pent: components 1 and 2 equally correspond to ^{1}ESA vectors (reflecting the biexponential decay observed from the time-resolved fluorescence measurements); components 3 and 4 similarly reflect the short- and long-lived ^{3}ESA vectors. Component 1 decays equally into components 3 and 4 with a rate k_1; components 2, 3, and 4 decay with a rate of k_2, k_3, k_4 respectively. Residual standard error 0.00175329.

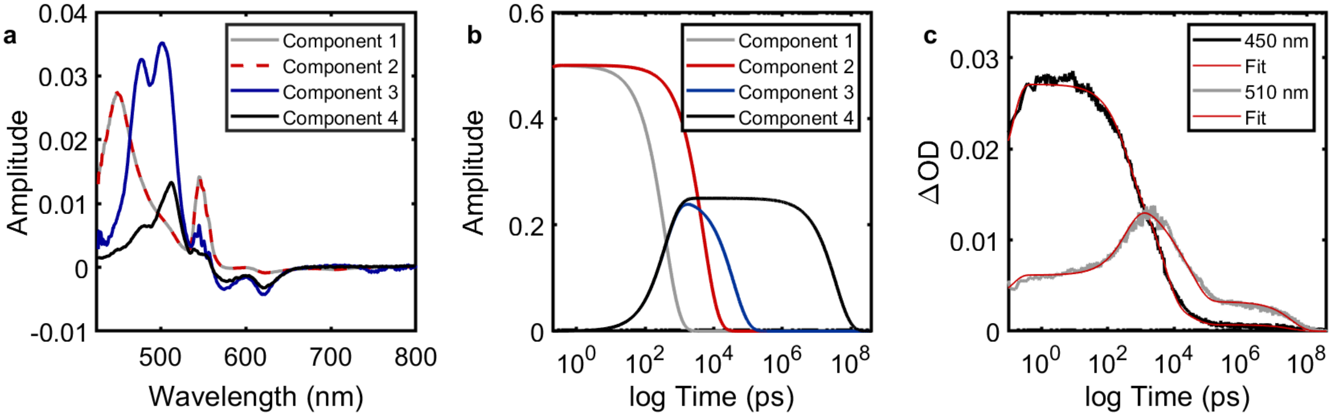

Figure A.21 Glotaran target analysis (Table A.1) of HDPP-Pent (50 µM, toluene) visible fs and ns TA data; no parameters fixed: (a) species associated spectra, (b) kinetic traces of fitted components, and (c) kinetic fits overlaying experimental data at 450 and 510 nm.

Table A.2 HDPP-Pent visible fs and ns TA target analysis; k_1 and k_2 fixed

	k (s^{-1})	Standard Error
k_1	$1.3(8) \times 10^9$	-
k_2	$8.5(0) \times 10^8$	-
k_3	$2.6(7) \times 10^7$	1.98×10^5
k_4	$2.8(7) \times 10^4$	3.37×10^2
	τ (ps)	
τ_1	$7.2(5) \times 10^2$	
τ_2	$1.1(8) \times 10^4$	
τ_3	$3.7(5) \times 10^4$	
τ_4	$3.4(8) \times 10^7$	

	1	2	3	4
1				
2		k_2		
3	k_1		k_3	
4	k_1			k_4

Fitted kinetic parameters obtained from a four-component model of the composite visible fs and ns TA data of HDPP-Pent: components 1 and 2 equally correspond to ^{1}ESA vectors (reflecting the biexponential decay observed from the time-resolved fluorescence measurements), components 3 and 4 similarly reflect the short- and long-lived ^{3}ESA vectors. Component 1 decays equally into components 3 and 4 with a rate k_1; components 2, 3, and 4 decay with a rate of k_2, k_3, k_4 respectively. k_1 and k_2 have been fixed given the rates from time-resolved fluorescence measurements. Residual standard error: 0.00176051.

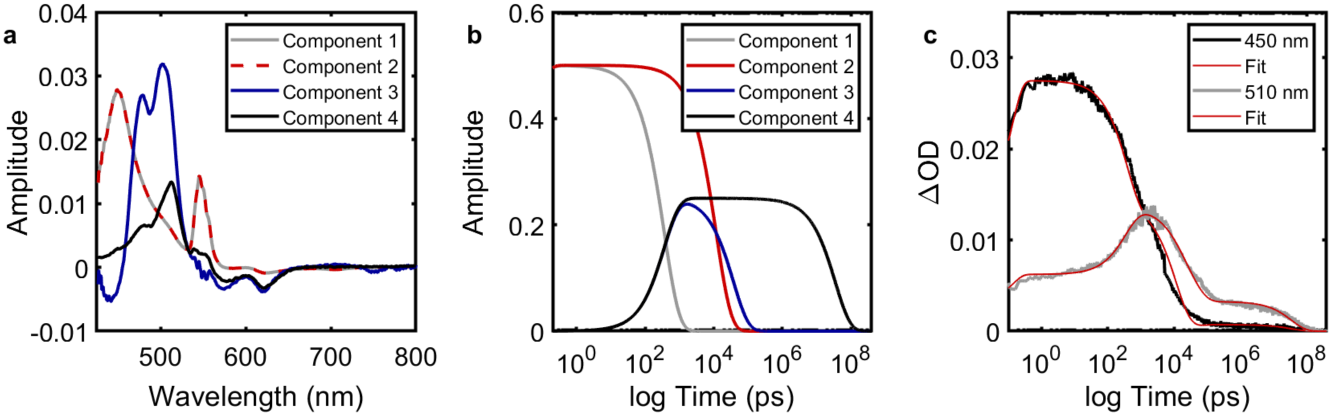

Figure A.22 Glotaran target analysis (Table A.2) of HDPP-Pent (50 µM, toluene) visible fs and ns TA data, k_1 and k_2 fixed: (a) species associated spectra, (b) kinetic traces of fitted components, and (c) kinetic fits overlaying experimental data at 450 and 510 nm.

Table A.3 HDPP-Pent visible fsTA target analysis

	k (s^{-1})	Standard Error
k_1	2.5(6) x 10^9	3.86 x 10^7
k_2	1.7(2) x 10^8	5.20 x 10^6
k_3	1.(8) x 10^7	1.72 x 10^6
	τ (ps)	
τ_1	3.9(1) x 10^2	
τ_2	5.8(1) x 10^3	
τ_3	5.(6) x 10^4	

	1	2	3
1			
2		k_2	
3	k_1		k_3

Fitted kinetic parameters obtained from a three-component model of the fsTA data of HDPP-Pent: components 1 and 2 equally correspond to ^{1}ESA vectors (reflecting the biexponential decay observed from the time-resolved fluorescence measurements); component 3 reflects the decay of the ^{3}ESA vector. Component 1 decays into component 3 with a rate k_1; components 2 and 3 decay with a rate of k_2 and k_3 respectively. Residual standard error: 0.00249052.

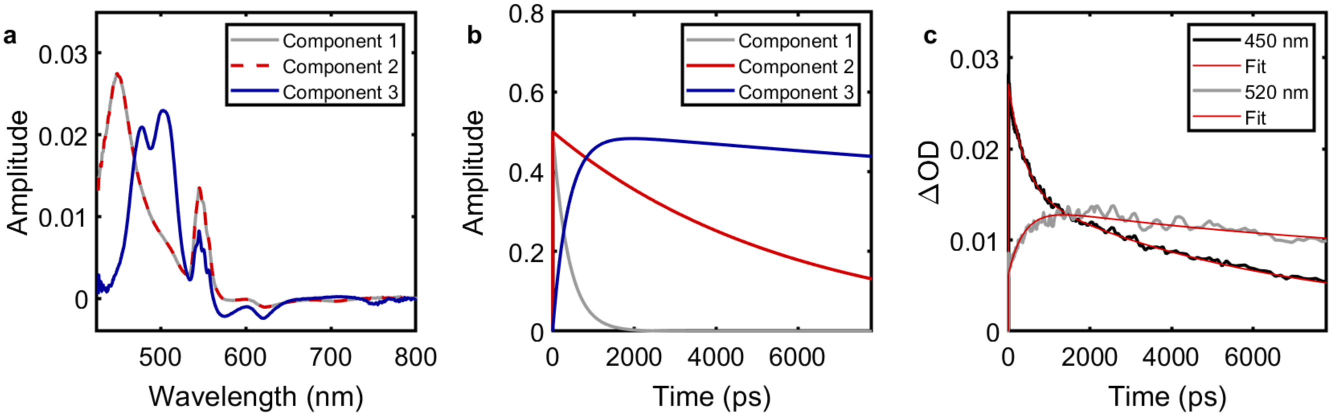

Figure A.23 Glotaran target analysis (Table A.3) of HDPP-Pent (50 µM, toluene) visible fsTA data: (a) species associated spectra, (b) kinetic traces of fitted components, and (c) kinetic fits overlaying experimental data at 450 and 510 nm.

Table A.4 HDPP-Pent nsTA target analysis

	k (s^{-1})	Standard Error
k_1	3.5(5) x 10^7	1.76 x 10^5
k_2	2.9(4) x 10^4	2.74 x 10^2
	τ (ns)	
$τ_1$	2.8(2) x 10^1	
$τ_2$	3.4(0) x 10^4	

	1	2
1	k_1	
2		k_2

Fitted kinetic parameters obtained from a three-component model of the nsTA data of HDPP-Pent: components 1 and 2 correspond to ^{3}ESA vectors representing the biexponential decay in the feature. Components 1 and 2 decay with rate constants k_1 and k_2 respectively. Residual standard error: 0.00197139.

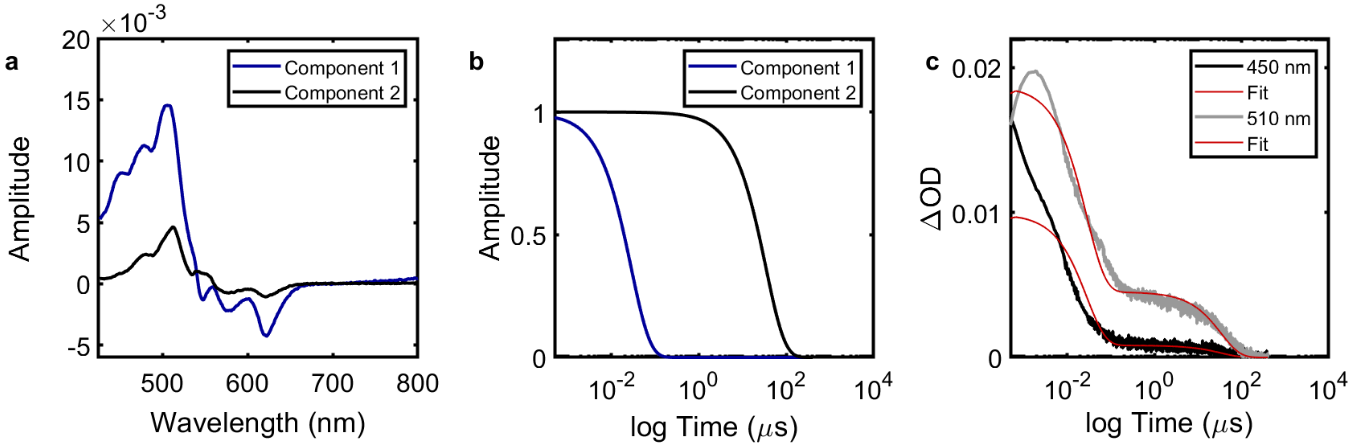

Figure A.24 Glotaran target analysis (Table A.4) of HDPP-Pent (50 µM, toluene) visible nsTA data: (a) species associated spectra, (b) kinetic traces of fitted components, and (c) kinetic fits overlaying experimental data at 450 and 510 nm.

Li$_2$(DPP-Pent)$_2$

Table A.5 Li$_2$(DPP-Pent)$_2$ visible fs and ns TA target analysis; 3-component model

	k (s^{-1})	Standard Error
k_1	1.0(4) x 10^{10}	1.47 x 10^{8}
k_2	4.3(0) x 10^{7}	2.44 x 10^{4}
k_3	2.8(6) x 10^{4}	2.84 x 10^{2}

	τ (ps)
τ_1	96.(2)
τ_2	2.3(3) x 10^{4}
τ_3	3.5(0) x 10^{7}

	1	2	3
1			
2	k_1	k_2	
3	k_1		k_3

Fitted kinetic parameters obtained from a three-component model of the composite fs and ns TA data of Li$_2$(DPP-Pent)$_2$: component 1 corresponds to a ^{1}ESA; components 2 and 3 reflect the short- and long-lived ^{3}ESA vectors. Component 1 decays equally into components 2 and 3 with a rate k_1; components 2 and 3 decay with a rate of k_2 and k_3 respectively. The final fits reported are averaged over two datasets. Residual standard error 0.00167259.

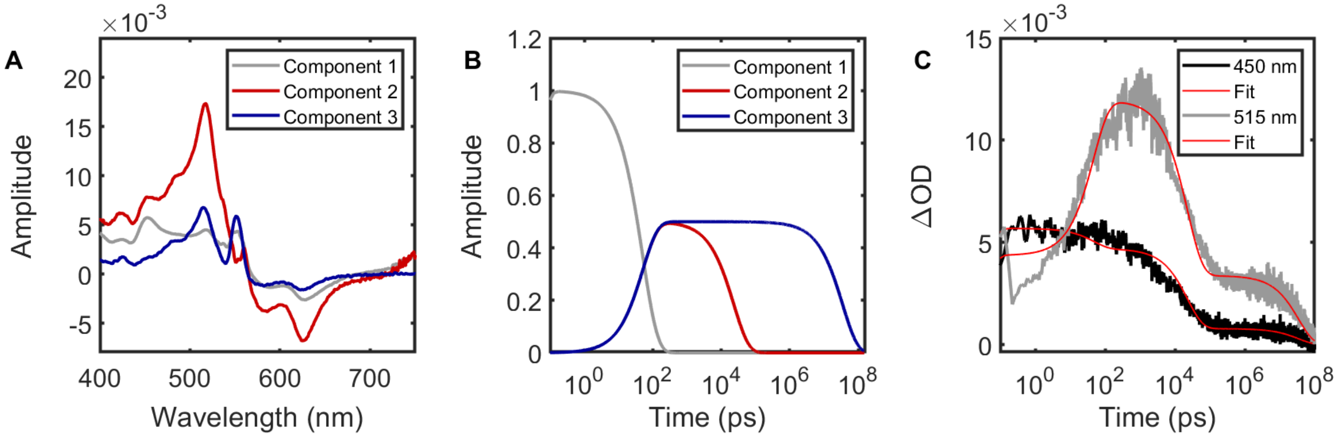

Figure A.25 Glotaran target analysis (Table A.5) of Li$_2$(DPP-Pent)$_2$ (50 µM, toluene) visible fs and ns TA data with a three-component model: (a) species associated spectra, (b) kinetic traces of fitted components, and (c) kinetic fits overlaying experimental data at 450 and 515 nm. The rapid rise of the triplet feature causes a slight deviation for the fits at these early times as seen in the intensity at 515 nm in the species associated spectra of component 1.

Table A.6 $Li_2(DPP\text{-}Pent)_2$ visible fs and ns TA target; 4-component model

	k (s^{-1})	Standard Error
k_1	9.0(4) x 10^{9}	9.66 x 10^{7}
k_2	9.3(9) x 10^{7}	2.75 x 10^{5}
k_3	7.(8) x 10^{6}	1.4 x 10^{5}
k_4	1.9(9) x 10^{4}	2.72 x 10^{2}

	τ (ps)
$τ_1$	1.1(1) x 10^{2}
$τ_2$	1.0(7) x 10^{4}
$τ_3$	1.(3) x 10^{5}
$τ_4$	5.0(3) x 10^{7}

	1	2	3	4
1				
2	k_1	k_2		
3	k_1		k_3	
4	k_1			k_4

Fitted kinetic parameters obtained from a four-component model of the composite fs and ns TA data of $Li_2(DPP\text{-}Pent)_2$: component 1 corresponds to a ^{1}ESA; components 2, 3, and 4 reflect short-, intermediate-, and long-lived ^{3}ESA vectors. Component 1 decays equally into components 2, 3, and 4 with a rate k_1; components 2, 3, and 4 decay with a rate of k_2, k_3, and k_4 respectively. The final fits reported are averaged over two datasets. Residual standard error 0.00167048.

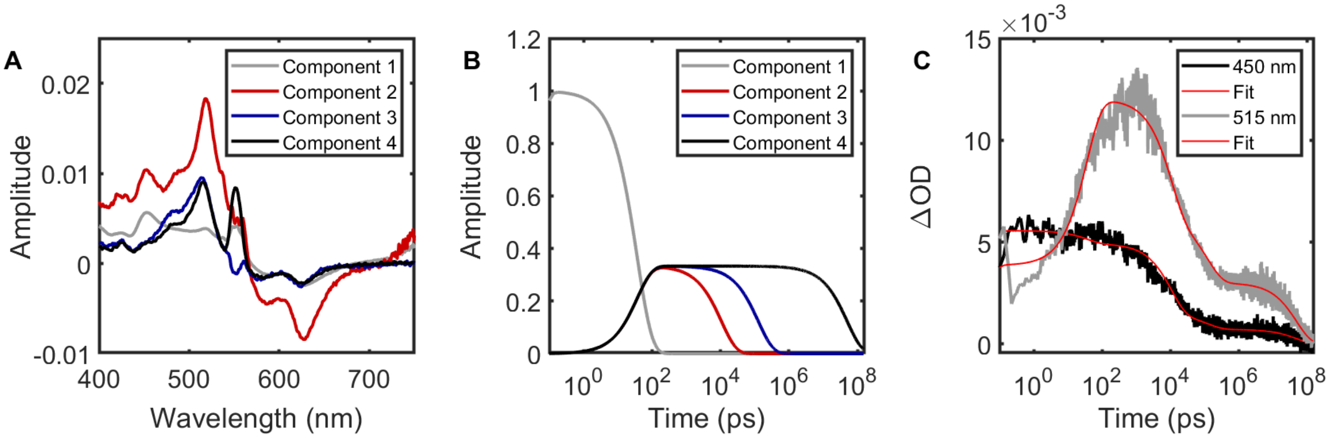

Figure A.26 Glotaran target analysis (Table A.6) of $Li_2(DPP\text{-}Pent)_2$ (50 µM, toluene) visible fs and ns TA data with a four-component model: (a) species associated spectra, (b) kinetic traces of fitted components, and (c) kinetic fits overlaying experimental data at 450 and 515 nm. The rapid rise of the triplet feature causes a slight deviation for the fits at these early times as seen in the intensity at 515 nm in the species associated spectra of component 1.

Table A.7 Li$_2$(DPP-Pent)$_2$ visible fsTA target analysis

	k (s^{-1})	Standard Error
k_1	1.44(0) x 10^{10}	8.786 x 10^{7}
k_2	2.8(6) x 10^{7}	3.25 x 10^{5}

	τ (ps)
τ_1	6.94(4) x 10^{1}
τ_2	2.51(1) x 10^{4}

	1	2
1		
2	k_1	k_2

Fitted kinetic parameters obtained from a two-component, sequential model of the fsTA data of Li$_2$(DPP-Pent)$_2$: component 1 corresponds to a ^{1}ESA, and component 2 reflects the ^{3}ESA vector. Residual standard error 0.00211332.

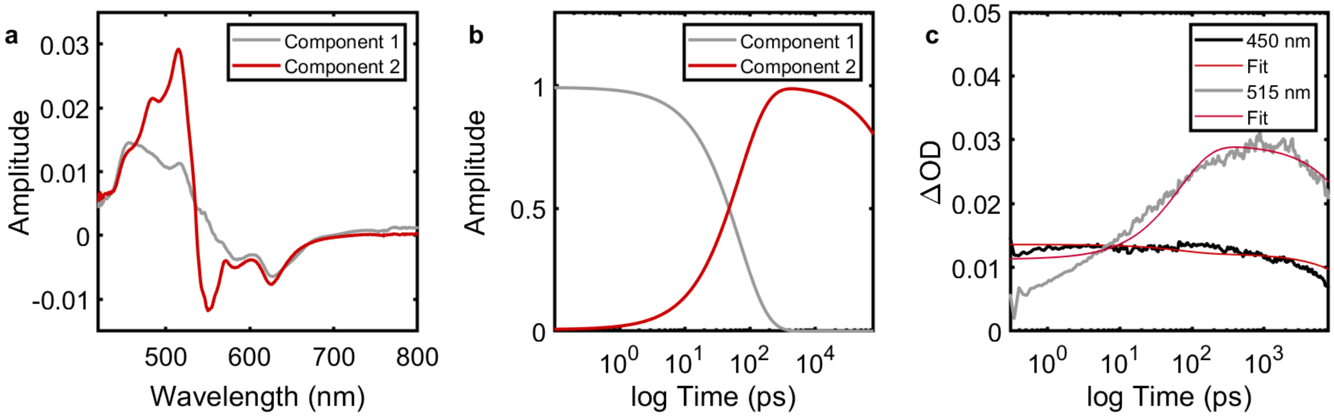

Figure A.27 Glotaran target analysis (Table A.7) of Li$_2$(DPP-Pent)$_2$ (50 µM, toluene) visible fsTA data: (a) evolution associated spectra, (b) kinetic traces of fitted components, and (c) kinetic fits overlaying experimental data at 450 and 510 nm. The rapid rise of the triplet feature causes a slight deviation for the fits at these early times as seen in the intensity at 515 nm in the species associated spectra of component 1.

Table A.8 Li$_2$(DPP-Pent)$_2$ visible nsTA target analysis

	k (s^{-1})	Standard Error
k_1	2.60(2) x 10^7	7.978 x 10^4
k_2	2.19(1) x 10^4	9.291 x 10^1
	τ (ns)	
$τ_1$	3.84(3) x 10^1	
$τ_2$	4.56(4) x 10^4	

$$\begin{array}{c|c|c|} & 1 & 2 \\ \hline 1 & k_1 & \\ \hline 2 & & k_2 \\ \hline \end{array}$$

Fitted kinetic parameters obtained from a two-component, sequential model of the nsTA data of Li$_2$(DPP-Pent)$_2$: components 1 and 2 correspond to the ^{3}ESA vector, reflecting a biexponential decay. Residual standard error 0.000664370.

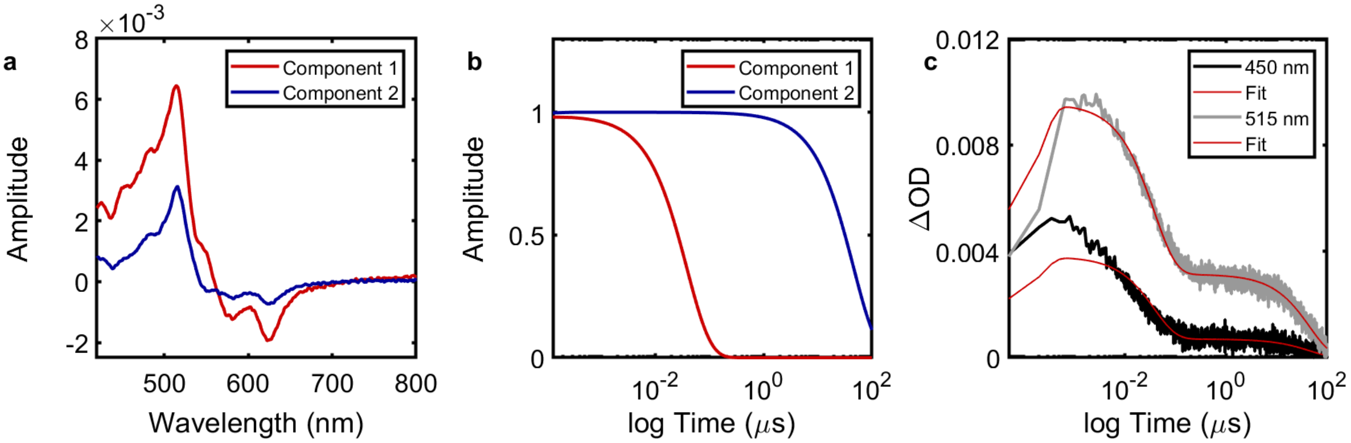

Figure A.28 Glotaran target analysis (Table A.8) of Li$_2$(DPP-Pent)$_2$ (50 µM, toluene) visible nsTA data: (a) species associated spectra, (b) kinetic traces of fitted components, and (c) kinetic fits overlaying experimental data at 450 and 510 nm.

KDPP-Pent

Table A.9 KDPP-Pent visible fs and ns TA target analysis – 3 components

	k (s^{-1})	Standard Error
k_1	1.60(0) x 10^9	9.897 x 10^6
k_2	1.75(3) x 10^8	5.121 x 10^5
k_3	6.0(5) x 10^4	1.6(5) x 10^2
	τ (ps)	
τ_1	6.25(0) x 10^2	
τ_2	5.70(5) x 10^4	
τ_3	1.6(5) x 10^7	

	1	2	3
1			
2	k_1	k_2	
3	k_1		k_3

Fitted kinetic parameters obtained from a three-component model of the composite fs and ns TA data of KDPP-Pent: component 1 corresponds to a ^{1}ESA; components 2 and 3 reflect the short- and long-lived ^{3}ESA vectors. Component 1 decays equally into components 2 and 3 with a rate k_1; components 2 and 3 decay with a rate of k_2 and k_3 respectively. Residual standard error 0.000864311.

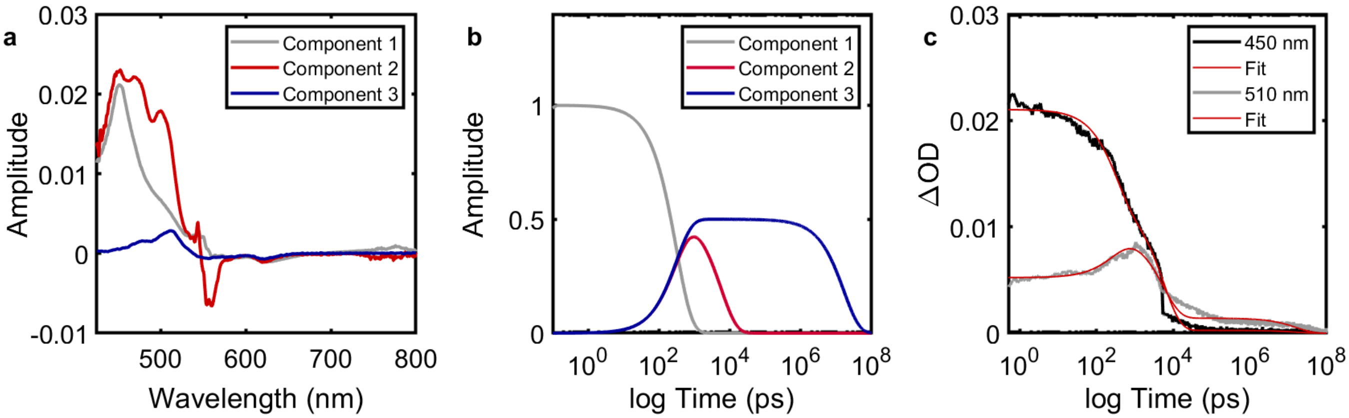

Figure A.29 Glotaran target analysis (Table A.9) of KDPP-Pent (50 µM, toluene) visible fs and nsTA data – three-component fit: (a) species associated spectra, (b) kinetic traces of fitted components, and (c) kinetic fits overlaying experimental data at 450 and 510 nm.

Table A.10 KDPP-Pent visible fs and ns TA target analysis – 4 components

	k (s^{-1})	Standard Error
k_1	2.2(5) x 10^9	1.71 x 10^7
k_2	2.7(5) x 10^8	2.14 x 10^6
k_3	8.7(1) x 10^7	4.85 x 10^5
k_4	3.7(2) x 10^4	4.85 x 10^2
	τ (ps)	
$τ_1$	4.4(4) x 10^2	
$τ_2$	3.6(4) x 10^4	
$τ_3$	1.1(5) x 10^5	
$τ_4$	2.6(9) x 10^7	

	1	2	3	4
1				
2		k_2		
3	k_1		k_3	
4	k_1			k_4

Fitted kinetic parameters obtained from a four-component model of the composite fs and ns TA data of KDPP-Pent: components 1 and 2 equally correspond to ^{1}ESA vectors; components 3 and 4 similarly reflect the short- and long-lived ^{3}ESA vectors. Component 1 decays equally into components 3 and 4 with a rate k_1; components 2, 3, and 4 decay with a rate of k_2, k_3, k_4 respectively. Residual standard error 0.000862214. k_1 and k_2 have been fixed given the rates from time-resolved fluorescence measurements.

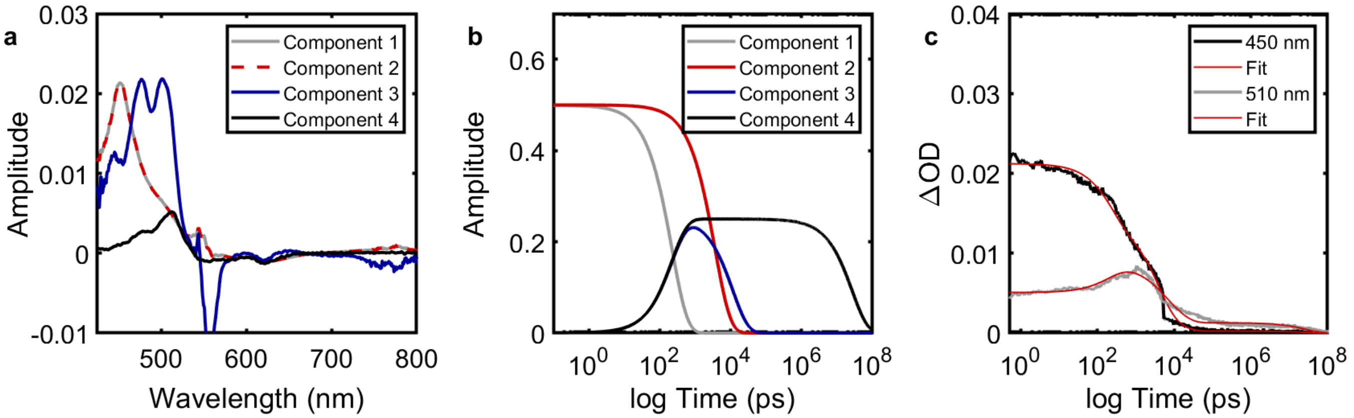

Figure A.30 Glotaran target analysis (Table A.10) of KDPP-Pent (50 µM, toluene) visible fs and nsTA data – four-component fit: (a) species associated spectra, (b) kinetic traces of fitted components, and (c) kinetic fits overlaying experimental data at 450 and 510 nm.

Table A.11 KDPP-Pent visible fsTA target analysis

	k (s^{-1})	Standard Error
k_1	2.2(7) x 10^9	2.86 x 10^7
k_2	1.4(4) x 10^8	1.14 x 10^6
	τ (ps)	
$τ_1$	4.4(1) x 10^2	
$τ_2$	6.9(4) x 10^3	

	1	2
1		
2	k_1	k_2

Fitted kinetic parameters obtained from a two-component, sequential decay model of the fsTA data of KDPP-Pent: components 1 and 2 correspond to the ^{1}ESA and ^{3}ESA vectors, respectively. Residual standard error 0.00179745.

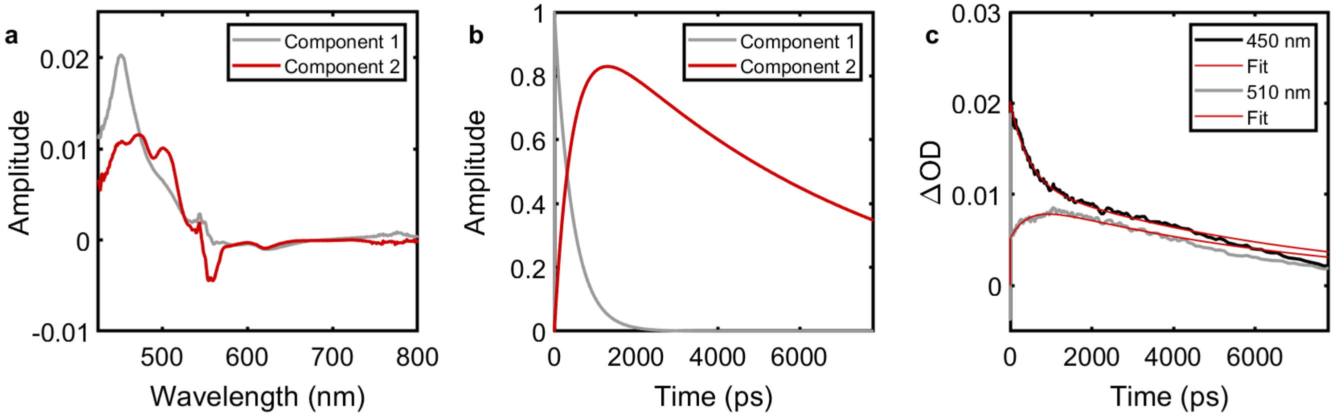

Figure A.31 Glotaran target analysis (Table A.11) of KDPP-Pent (50 µM, toluene) visible fsTA data: (a) evolution associated spectra, (b) kinetic traces of fitted components, and (c) kinetic fits overlaying experimental data at 450 and 510 nm.

Table A.12 KDPP-Pent visible nsTA target analysis

	k (s^{-1})	Standard Error
k_1	3.1(6) x 10^7	1.27 x 10^5
k_2	2.7(3) x 10^4	1.14 x 10^2
	τ (ns)	
$τ_1$	3.1(6) x 10^1	
$τ_2$	3.6(6) x 10^4	

	1	2
1	k_1	
2		k_2

Fitted kinetic parameters obtained from a two-component, parallel decay model of the nsTA data of KDPP-Pent: components 1 and 2 correspond to the ^{3}ESA vectors. Residual standard error 0.000674488.

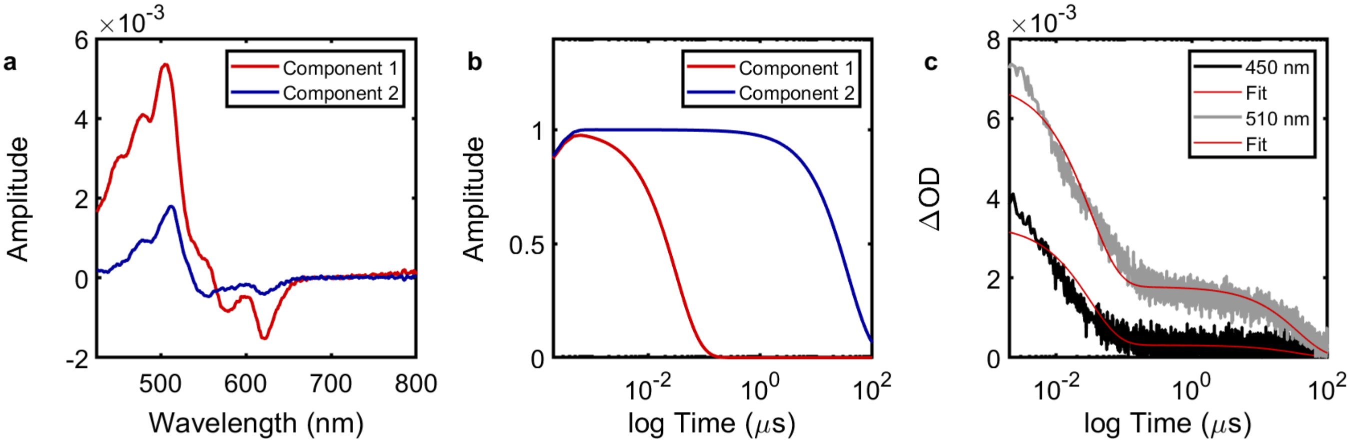

Figure A.32 Glotaran target analysis (Table A.12) of KDPP-Pent (50 µM, toluene) visible nsTA data: (a) evolution associated spectra, (b) kinetic traces of fitted components, and (c) kinetic fits overlaying experimental data at 450 and 510 nm.

VIII. HDPP-Pent: Triplet Extinction Coefficient Estimation

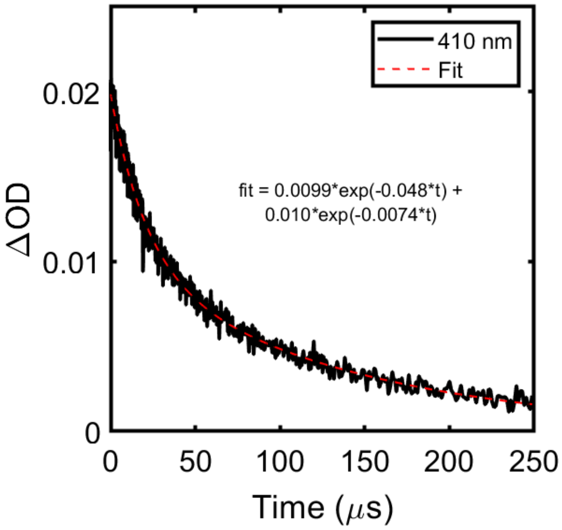

Figure A.33 Anthracene (500 µM, toluene) ^{3}ESA ns transient absorption trace at 410 nm.

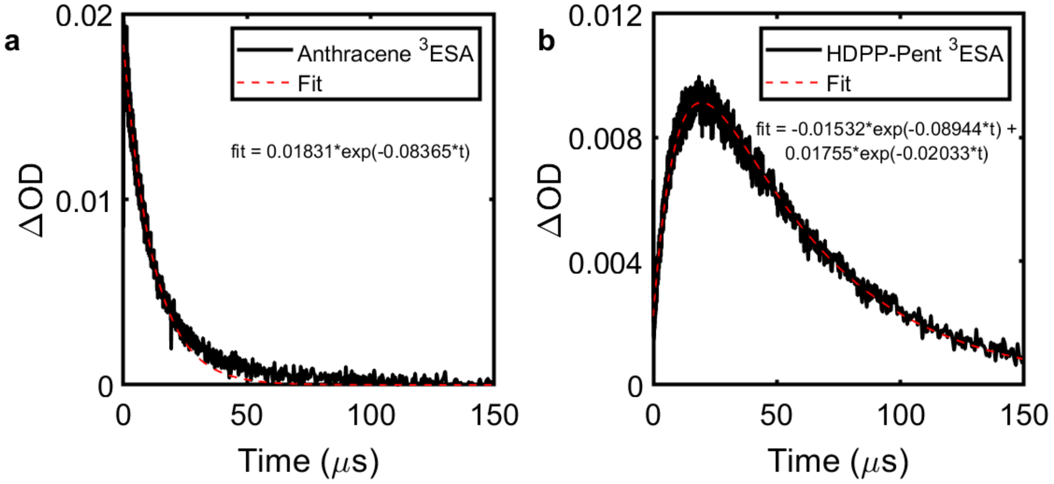

Figure A.34 Photosensitization experiment (500 μM Anthracene, 10 μM HDPP-Pent in toluene): (a) Anthracene ^{3}ESA nsTA kinetic trace at 410 nm, (b) HDPP-Pent ^{3}ESA nsTA kinetic trace at 510 nm.

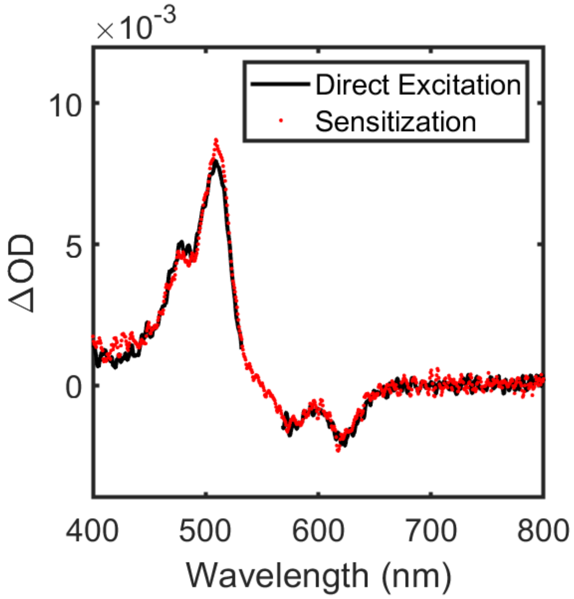

Figure A.35 Comparison between the transient absorption spectrum of HDPP-Pent at long delay times (50 ns) after direct photosensitization with 550 nm light and the transient absorption spectrum of the photosensitized anthracene (500 μM) and HDPP-Pent (10 μM) after exciting anthracene at 360 nm at delay times (35 μs) past the decay of the anthracene triplet ESA. In the photosensitization experiment, we expect the anthracene triplet to be transferred to HDPP-Pent, resulting in the observation of the triplet transient absorption spectrum of HDPP-Pent at long delay times. This same spectrum is observed in the direct excitation experiment at long delay times, indicating that these spectral features are indeed associated with the HDPP-Pent T_1 state. The residual pump scatter at 550 nm was excised from the direct excitation spectrum.

The Anthracene (500 μM) and HDPP-Pent (10 μM) photosensitization experiment will be used to demonstrate the calculation of the HDPP-Pent ^{3}ESA extinction coefficient given the reported Anthracene ^{3}ESA molar absorptivity (42,000 M^{-1} cm^{-1}).[4–7] This is accomplished by setting the concentrations of Anthracene and HDPP-Pent triplets to be equal in the Beer-Lambert regime and solving for ^{3}HDPP-Pent ε as in Equation 2:

$$c_{\,^3Anth} = c_{\,^3HDPP-Pent}$$

$$\frac{\Delta OD_{\,^3Anth}}{\varepsilon_{\,^3Anth} \cdot l} = \frac{\Delta OD_{\,^3HDPP-Pent}}{\varepsilon_{\,^3HDPP-Pent} \cdot l}$$

$$\varepsilon_{\,^3HDPP-Pent} = \frac{\Delta OD_{\,^3HDPP-Pent}}{\Delta OD_{\,^3Anth}} \cdot \varepsilon_{\,^3Anth} \qquad Eq\ (2)$$

The assumption underlying this equation is that the energy transfer efficiency is near unity – that the concentration of anthracene triplets fully transfers into HDPP-Pent triplets. In order to fulfill this estimation, corrections must be made to the ^{3} HDPP-Pent ΔOD to account for triplet transfer efficiency (Φ_{ET}) and the relative rate of the rise and decay of the HDPP-Pent ^{3}ESA ($\Phi_{T(decay)}$).

$$\Phi_{ET} = \frac{k_{sens}}{k_{sens} + k_{intrinsic}}$$

$$\Phi_{ET} = \frac{0.08365}{0.08365 + 0.048} = 0.64$$

$$\Phi_{T(decay)} = \frac{k_{T(rise)}}{k_{T(rise)} + k_{T(decay)}}$$

$$\Phi_{T(decay)} = \frac{0.08944}{0.08944 + 0.02033} = 0.81$$

The corrected ^{3}HDPP-Pent ΔOD (ΔOD$_{corr}$) can thus be estimated and the HDPP-Pent ^{3}ESA extinction coefficient can be calculated as in Equation 2:

$$\Delta OD_{corr} = \frac{\Delta OD_{\ ^3HDPP-Pent}}{\Phi_{ET} \cdot \Phi_{T(decay)}} = \frac{0.0091}{0.64 \cdot 0.81}$$

$$\Delta OD_{corr} = 0.0176$$

$$\varepsilon_{\ ^3HDPP-Pent} = \frac{0.0176}{0.0183} \cdot (42{,}000\ M^{-1}cm^{-1})$$

$$\varepsilon_{\ ^3HDPP-Pent} = 40{,}393\ M^{-1}cm^{-1}$$

This process is repeated for each concentration of HDPP-Pent (10, 20, 50, 100 μM) and the results are compiled in Figure S35. As can be seen, the calculated ^{3}HDPP-Pent extinction coefficient approaches a limit of ~ 49,000 M^{-1} cm^{-1} as the concentration of HDPP-Pent is increased (i.e. the triplet energy transfer efficiency approaches unity).

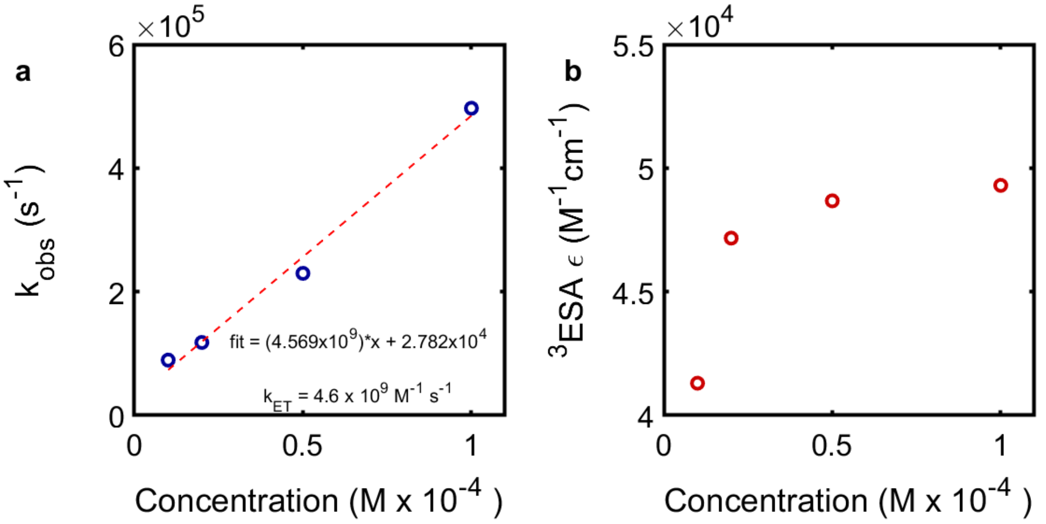

Figure A.36 Concentration-dependent photosensitization experiments between Anthracene (500 μM) and HDPP-Pent (X μM, X = 10, 20, 50, 100): (a) observed energy transfer rate (k_{obs}) vs. HDPP-Pent concentration, fitted to a linear function, the slope of which gives the bimolecular rate constant (k_{ET}); (b) calculated HDPP-Pent ^{3}ESA extinction coefficient vs. HDPP-Pent concentration.

IX. HDPP-Pent: Triplet Yield Estimation

In order to estimate the triplet yield, we can use Equation 3. As a note, we refer to [T_1] as the concentration of excited triplet states without differentiation between triplet pair (T_1T_1) and free triplet (T_1) states.

$$Triplet\ \%\ Yield = \frac{[T_1]}{[S_1]} \cdot 100 \qquad Eq\ (3)$$

i. Concentration of Excited Singlets

Let us first consider the maximum concentration of excited singlets generated. This has been previously estimated using the ground state bleach (GSB) feature. However, it must be noted in the case of HDPP-Pent that the shape and intensity of the GSB changes over the course of the transient absorption experiment in a way that suggests there is a complex overlap of GSB and ESA features in the spectrum. This makes the GSB unreliable in the evaluation of the triplet yield. The concentration of excited singlets may alternatively be estimated as the product of the number of photons per pulse and the ratio of pump intensity before and after the sample (I/I_0) divided by the product of Avogadro's number (N_A) and the excitation volume (V):[8]

$$[\boldsymbol{S_1}] = \frac{\left(\frac{\boldsymbol{photons}}{\boldsymbol{pulse}}\right) \cdot \left(\frac{\boldsymbol{I}}{\boldsymbol{I_0}}\right)}{\boldsymbol{N_A} \cdot \boldsymbol{V}}$$

$$\left(\frac{photons}{pulse}\right) = \frac{power}{(rep\ rate) \cdot \left(\frac{energy}{photon}\right)}$$

$$\left(\frac{I}{I_0}\right) = 1 - 10^{-A}$$

$$V = \pi r^2 l$$

Each component may be first evaluated individually. The photons per pulse can be derived from the excitation power (100 μW), the laser repetition rate (1000 s^{-1}), and the energy per photon (as calculated by the product of Planck's constant h and the frequency of 550 nm light). I/I_0 can be calculated as the difference from unity of ten raised to the negative power of the sample absorbance at 550 nm (0.11). The excitation volume is assumed to be cylindrical using the radius of the excitation spot (0.013 cm) and the path length of the sample (0.2 cm).

$$\left(\frac{photons}{pulse}\right) = \frac{1 \times 10^{-4}\, W}{(1{,}000\, s^{-1}) \cdot (3.61 \times 10^{-19}\, J)} = 2.77 \times 10^{11}\, pulse^{-1}$$

$$\left(\frac{I}{I_0}\right) = 1 - 10^{-0.11} = 0.2238$$

$$V = \pi \cdot (1.30 \times 10^{-2}\, cm)^{2} \cdot (0.2\, cm) \cdot (0.001\, L\, cm^{-3}) = 1.06 \times 10^{-7}\, L$$

$$[S_1] = \frac{(2.77 \times 10^{11}) \cdot (0.2238)}{(6.022 \times 10^{23}) \cdot (1.06 \times 10^{-7})} = 9.7 \times 10^{-7}\, M$$

ii. Concentration of Excited Triplets

The concentration of HDPP-Pent triplets may be estimated from the extinction coefficient of the ^{3}ESA at 510 nm as derived above and the maximum ΔOD value at 510 nm from the experimental transient absorption data. However, from the time-resolved luminescence data and the target fitting, it is apparent that when the TA ^{3}ESA at 510 nm reaches its maximum intensity (t ~ 1.4 ns), there is contribution to this intensity from the ^{1}ESA. The fit may be used to decompose the ΔOD at 510 nm to its contributions from the ^{1}ESA and ^{3}ESA, and the triplet contribution may be used to estimate the corrected triplet yield.

The target fitting as shown in Figure S21 gives a maximum ΔOD_{510nm} of 0.0128. The contributions of the different component vectors to the target fit can be decomposed from the kinetic traces (Figure S21b), which provides a weighting coefficient or effective concentration for each vector at 1.4 ns. The SAS (Figure S21a) provides the relative molar extinction of each vector at 510 nm. Taking the weighted sum of the first and second vectors gives the ΔOD contribution of the ^{1}ESA at 510 nm. Likewise, taking the weighted sum of the third and fourth vectors gives the relative ΔOD contribution of the ^{3}ESA. These values are collected in Table S12.

Table A.13 Estimation of ^{1}ESA and ^{3}ESA ΔOD contributions at 510 nm in the transient absorption spectrum of HDPP-Pent (50 μM, toluene).

component	1	2	3	4
Relative contribution at 1.4 ns	0.0103	0.4437	0.2379	0.2448
Intensity of SAS at 510 nm	0.0062	0.0062	0.0285	0.0180
	^{1}ESA		^{3}ESA	
ΔOD_{510nm} contribution at 1.4 ns	0.0028		0.010	

The maximum concentration of triplets can then be estimated in the Beer-Lambert regime and the triplet yield can be thus calculated.

$$[T_1] = \frac{\Delta OD_{510nm}}{\varepsilon_{\,^3DPP-Pent} \cdot l}$$

$$[T_1] = \frac{0.010}{(49{,}000) \cdot (0.2)} = 1.0 \times 10^{-6}\, M$$

$$Triplet\ Yield = \frac{[T_1]}{[S_1]} \cdot 100 = \frac{1.0 \times 10^{-6}\, M}{9.7 \times 10^{-7}\, M} \cdot 100$$

$$Triplet\ Yield \sim 100\ \%$$

X. $Li_2(DPP\text{-}Pent)_2$: Triplet Extinction Coefficient Estimation

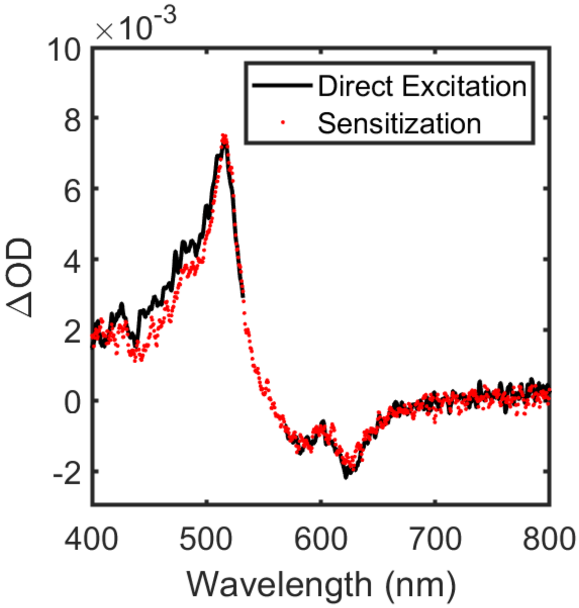

Figure A.37 Comparison between the transient absorption spectrum of $Li_2(DPP\text{-}Pent)_2$ at long delay times (20 ns) after direct photosensitization with 550 nm light and the transient absorption spectrum of the photosensitized anthracene (500 µM) and $Li_2(DPP\text{-}Pent)_2$ (50 µM) after exciting anthracene at 360 nm at delay times (100 µs) past the decay of the anthracene triplet ESA. In the photosensitization experiment, we expect the anthracene triplet to be transferred to $Li_2(DPP\text{-}Pent)_2$, resulting in the observation of the triplet transient absorption spectrum of $Li_2(DPP\text{-}Pent)_2$ at long delay times. This same spectrum is observed in the direct excitation experiment at long delay times, indicating that these spectral features are indeed associated with the $Li_2(DPP\text{-}Pent)_2$ T_1 state. The residual pump scatter at 550 nm was excised from the direct excitation spectrum.

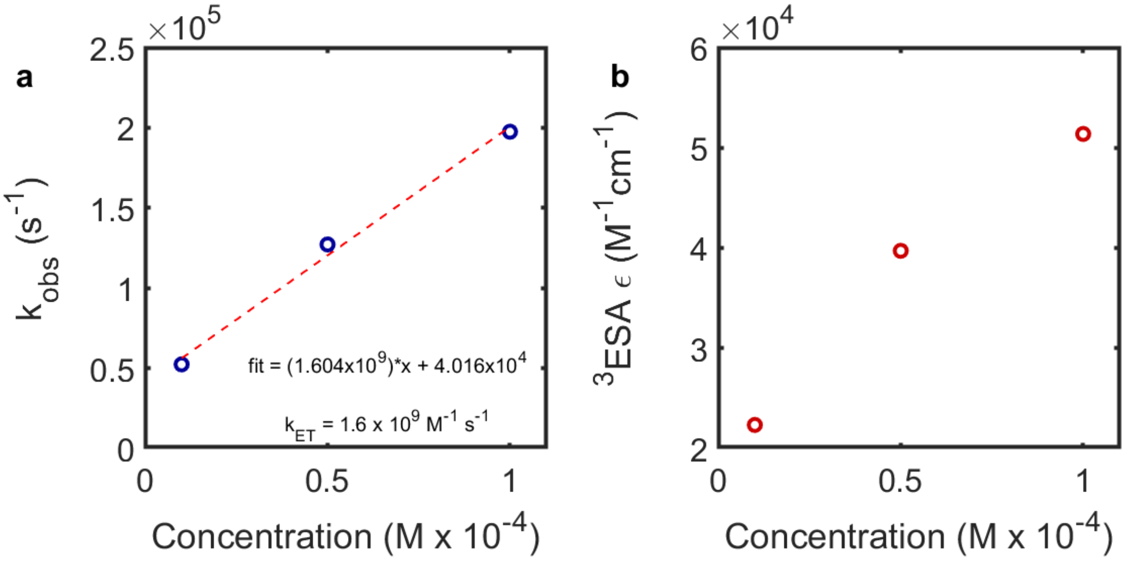

Figure A.38 Concentration-dependent photosensitization experiments between Anthracene (500 µM) and Li_2(DPP-Pent)$_2$ (X µM, X = 10, 50, 100): (a) observed energy transfer rate (k_{obs}) vs. Li_2(DPP-Pent)$_2$ concentration (based on formula weight), fitted to a linear function, the slope of which gives the bimolecular rate constant (k_{ET}); (b) calculated Li_2(DPP-Pent)$_2$ ^{3}ESA extinction coefficient vs. Li_2(DPP-Pent)$_2$ concentration.

XI. $Li_2(DPP\text{-}Pent)_2$: Triplet Yield Estimation

i. Method: extinction coefficient

As with HDPP-Pent, the concentration of excited singlets is first estimated using the energy of the 550 nm pump excitation, the absorbance of the sample at 550 nm (0.0711), and the excitation volume (1.06 x 10^{-7} L).

$$[S_1] = \frac{(2.77\ \times 10^{11}) \cdot (0.1489)}{(6.022\ \times\ 10^{23}) \cdot (1.06\ \times\ 10^{-7})} = 6.5\ \times\ 10^{-7}\ M$$

As we do not have evidence to suggest there is significant singlet population overlapped with the triplet ESA at its maximum in the TA data of $Li_2(DPP\text{-}Pent)_2$, we directly estimate the triplet yield without correction from the fitted data.

$$[T_1] = \frac{\Delta OD_{510nm}}{\varepsilon\ {}^{3}{}_{LiDPP-Pent} \cdot l}$$

$$[T_1] = \frac{0.013}{(52{,}000) \cdot (0.2)} = 1.27\ \times\ 10^{-6}\ M$$

$$Triplet\ Yield = \frac{[T_1]}{[S_1]} \cdot 100 = \frac{1.27\ \times\ 10^{-6}\ M}{9.7\ \times\ 10^{-7}\ M} \cdot 100$$

$$Triplet\ Yield \sim 195\ \%$$

ii. Method: ground state bleach

We can estimate the triplet yield in $Li_2(DPP\text{-}Pent)_2$ via the ground state bleach in the method of Eaton et al.[9] The percentage of excited molecules estimated from the energy density of the 550 nm pump is approximately 1.1%, and using the ground state absorbance at 625 nm (0.2), we can estimate the expected ground state bleach intensity of -0.0022. From this we can estimate a triplet yield of ~ 186%.

$$Predicted\ Max\ \Delta OD_{625\ nm} = -2.2\ mOD$$

$$Experimental\ Max\ \Delta OD_{625\ nm} = -4.1\ mOD$$

$$Triplet\ Yield = \frac{-4.1}{-2.2} \cdot 100 \sim 186\ \%$$

XII. Comparison Between Singlet Fission Rates and Triplet Lifetimes

Table A.14 Comparison between singlet fission (τ_{SF}) and triplet lifetimes (τ_T) for HDPP-Pent, Li_2(DPP-Pent)$_2$, KDPP-Pent, and previously reported bipentacene systems *ortho*-**2**, *meta*-**2**, and *para*-**2** (in benzonitrile),[10] BP0, BP1, BP2,[11] TFM, BCO, Spi, and EBD (in chloroform),[12] PD, and PT.[13] The compounds are referenced using the moniker given in their respective texts, and structures are provided for each following the table. Here, τ_T is used generally for the fitted lifetimes of the triplet features in the transient absorption spectrum, encompassing both ^{M}(TT) – the shorter lifetime(s) – and uncorrelated triplet lifetimes where applicable. A comprehensive review of lifetimes in covalently linked dimers appears in Korovina et al.[14]

	τ_{SF}	τ_T
ortho-**2**	500 fs	12 ps
meta-**2**	63 ps	2.2 ns
para-**2**	2.7 ps	17.3 ps
BP0	760 fs	450 ps
BP1	20 ps	16.5 ns
BP2	220 ps	270 ns (1)
TFM	49.7 ps	531 ns (1), 23.0 μs (2)
BCO	20 ns	1.8 μs (1), 18.0 μs (2)
Spi	54.5 ps	705 ns (1), 19.6 μs (2)
EBD	10.4 ps	174 ns (1), 24.3 μs (2)
PD	435 ps	8.3 ns (1); 87 ns (2); 25 μs (3)
PT	147 ps	12 ns (1); 70 ns (2); 32 μs (3)
HDPP-Pent	730 ps	38 ns (1); 36 μs (2)
Li_2(DPP-Pent)$_2$	100 ps	23 ns (1); 35 μs (2)
KDPP-Pent	400 – 600 ps	12 ns (1); 27 μs (2)

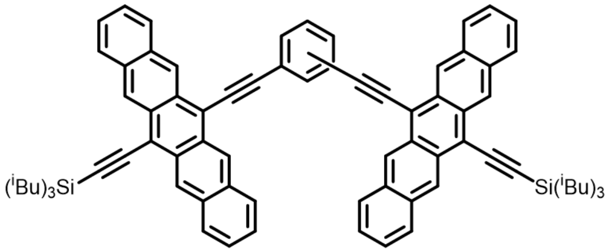

*ortho-, meta-, and para-***1**

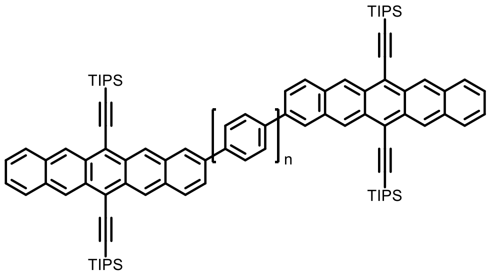

BPn (n=0,1,2)

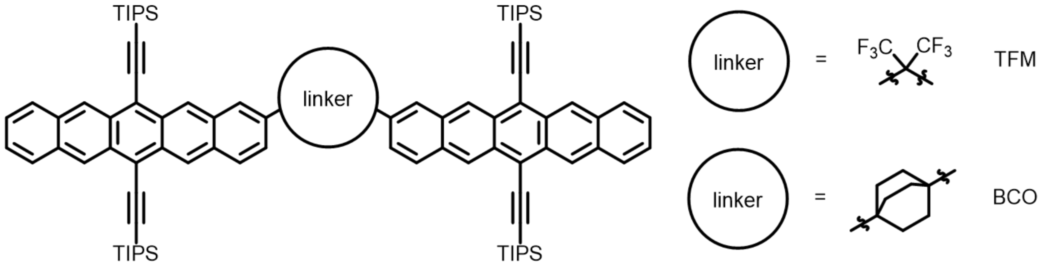

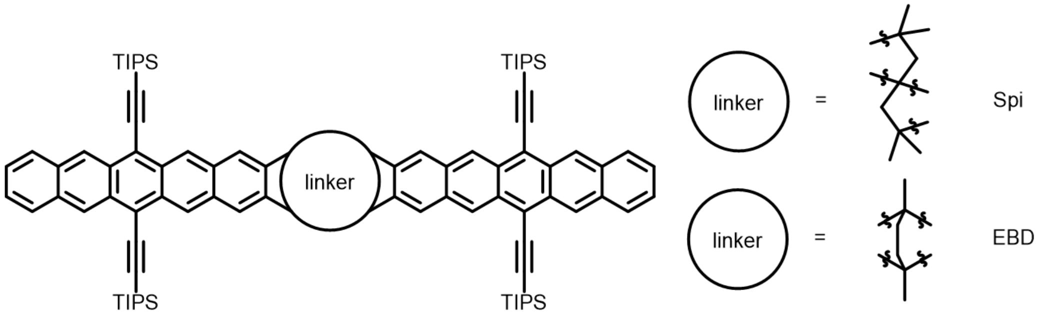

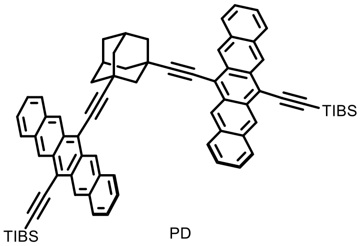

PD

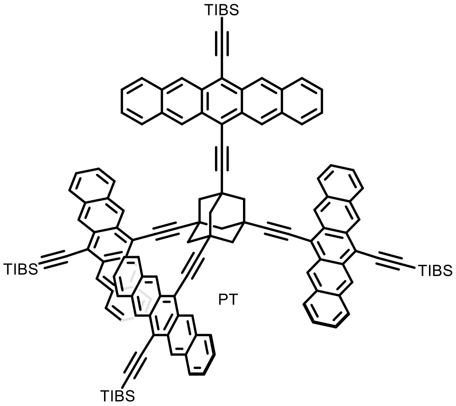

PT

XIII. ^{1}H and ^{13}C NMR

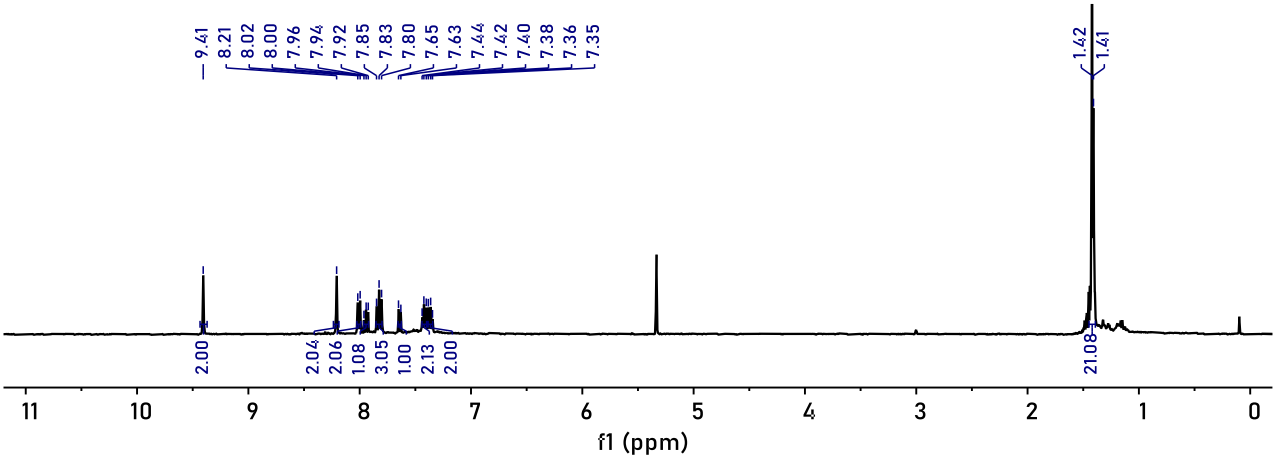

Figure A.39 ^{1}H NMR spectrum of PentPyBr (400 MHz, CDCl$_3$).

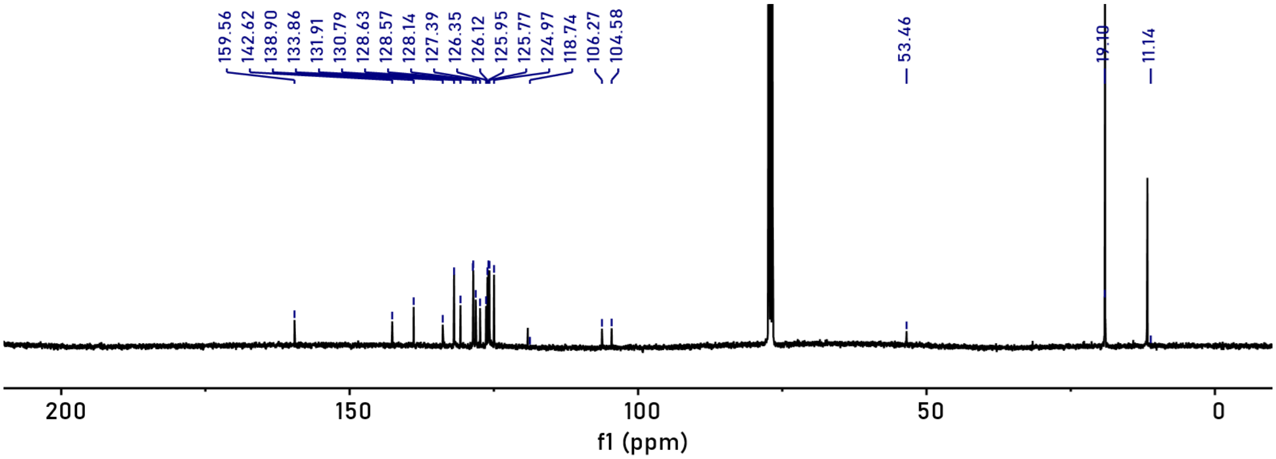

Figure A.40 ^{13}C NMR spectrum of PentPyBr (400 MHz, $CDCl_3$).

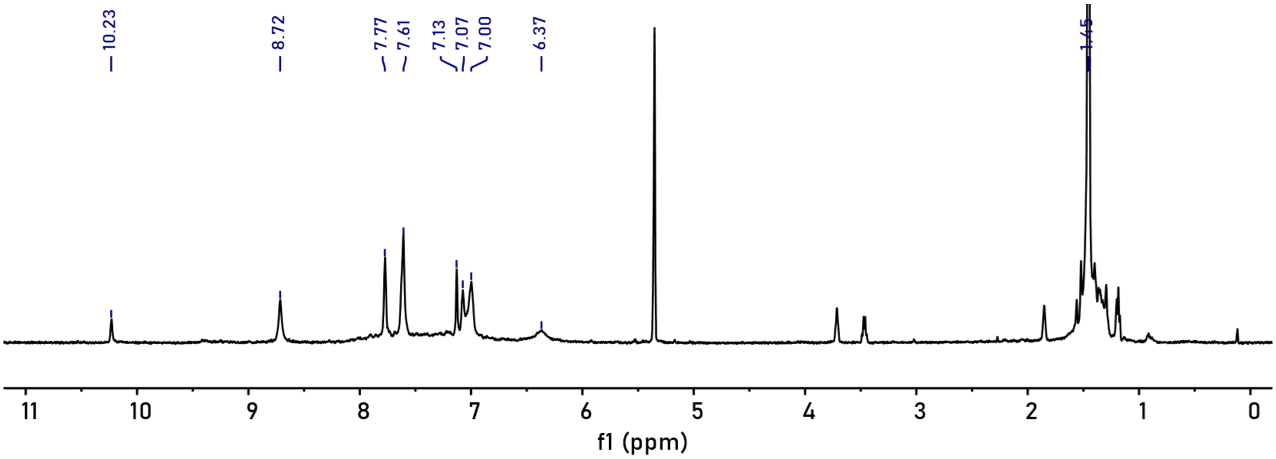

Figure A.41 ^{1}H NMR spectrum of HDPP-Pent (400 MHz, CD_2Cl_2).

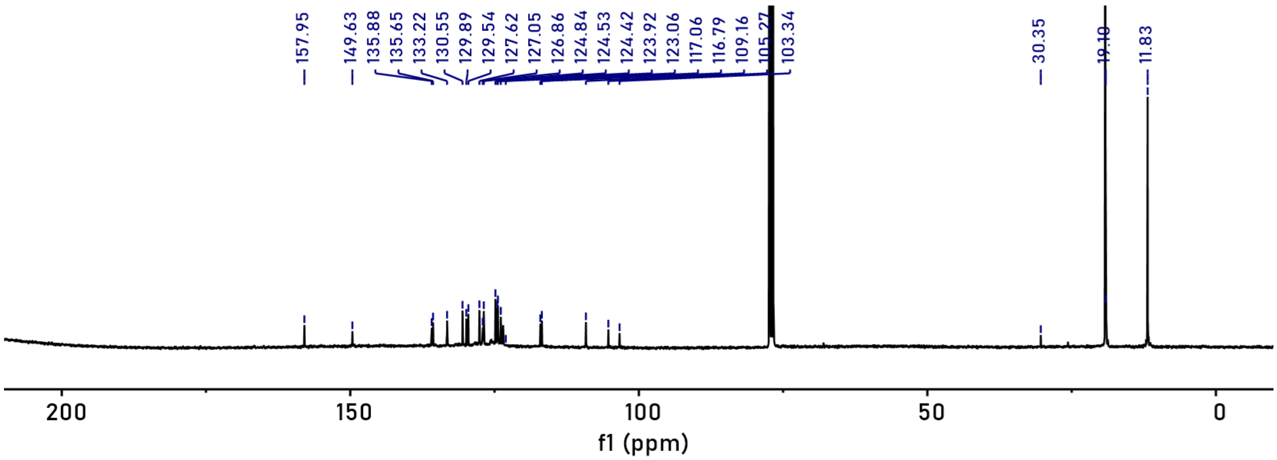

Figure A.42 ^{13}C NMR spectrum of HDPP-Pent (400 MHz, CDCl$_3$).

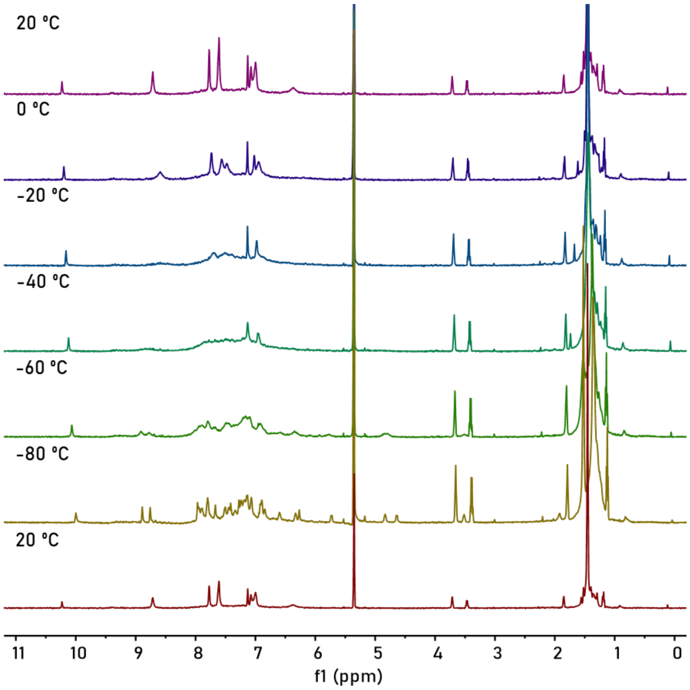

Figure A.43 Variable temperature ^{1}H NMR spectra of HDPP-Pent (400 MHz, CD_2Cl_2).

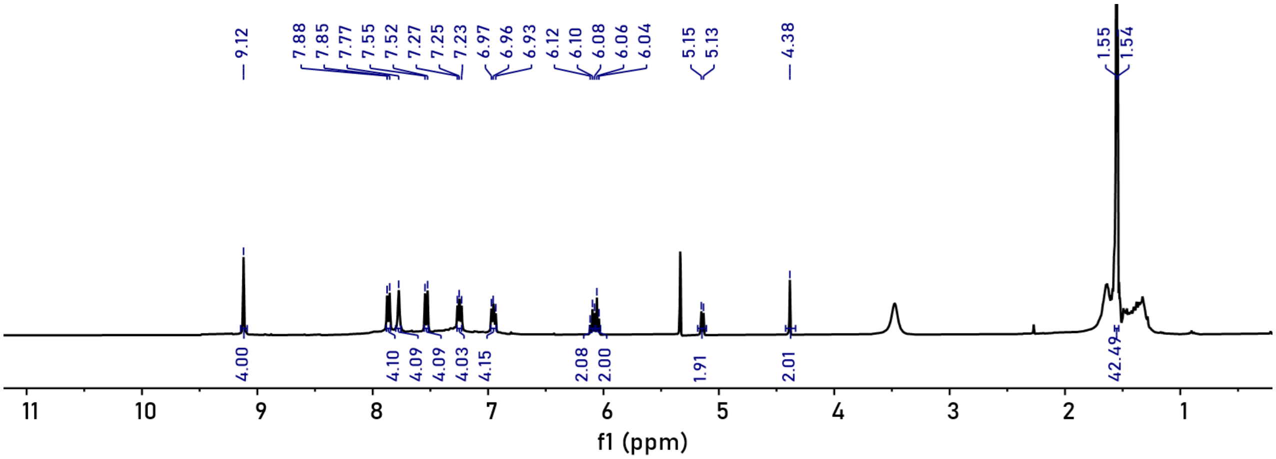

Figure A.44 ^{1}H NMR spectrum of Li_2(DPP-Pent)$_2$ (400 MHz, CD_2Cl_2).

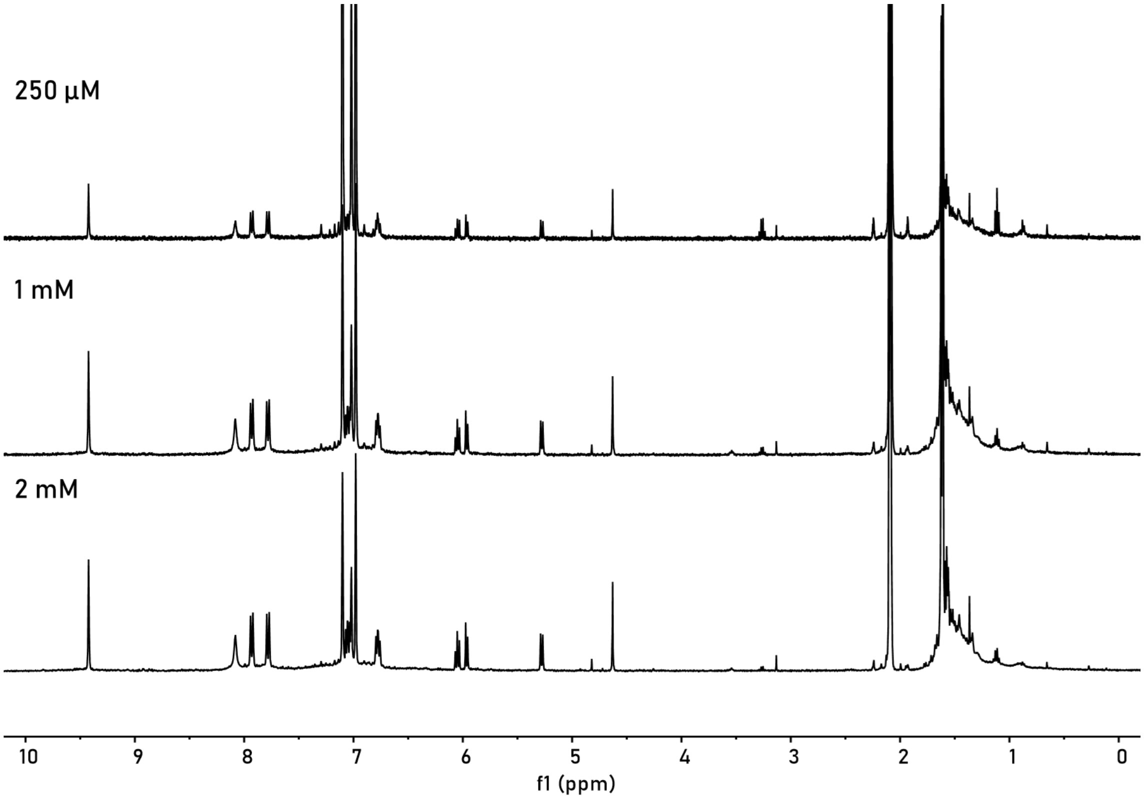

Figure A.45 ^{1}H NMR spectrum of Li_2(DPP-Pent)$_2$ at different concentrations in toluene-d8 (400 MHz, toluene-d8).

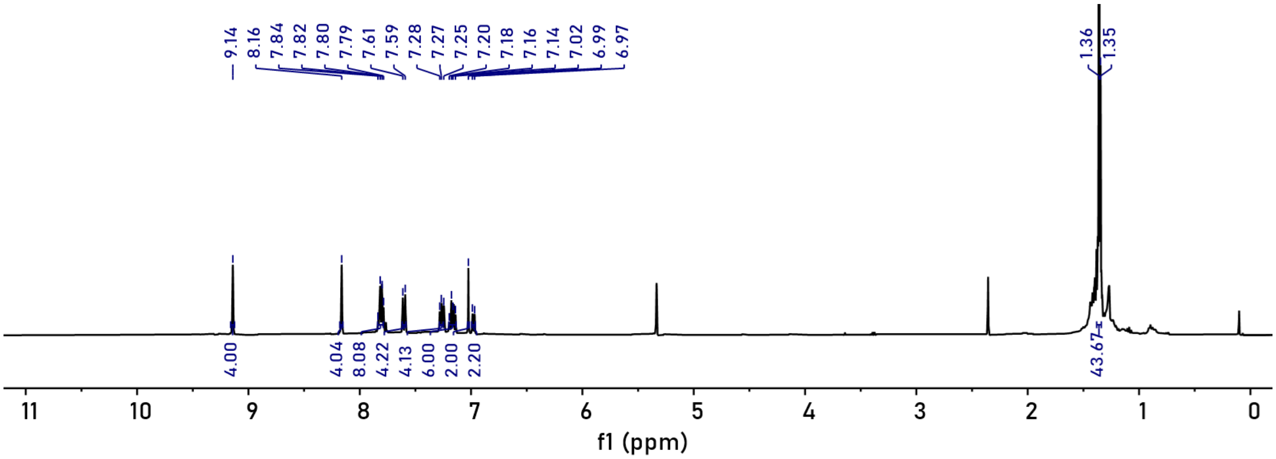

Figure A.46 ^{1}H NMR spectrum of KDPP-Pent (400 MHz, CD_2Cl_2).

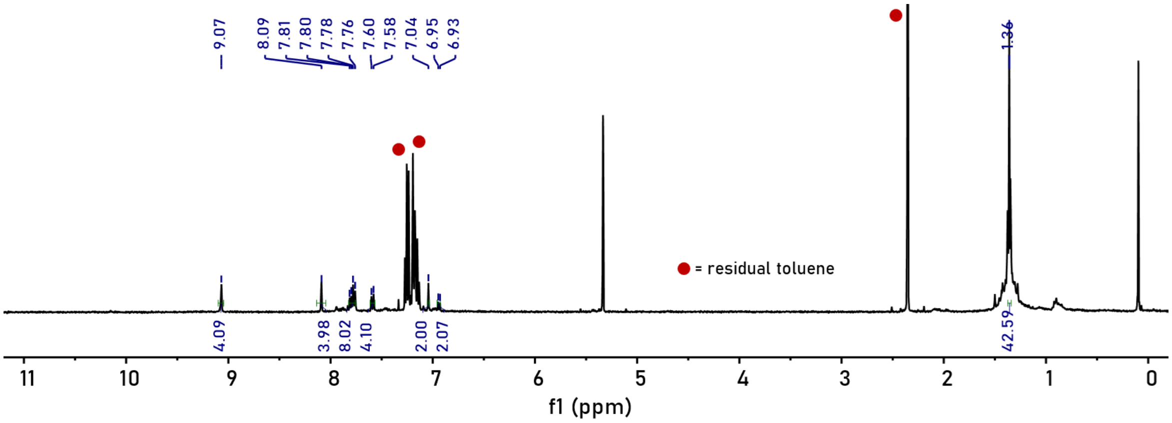

Figure A.47 ^{1}H NMR spectrum of NaDPP-Pent (400 MHz, CD_2Cl_2). A significant amount of toluene (peaks at 2.34, 7.14, 7.24 ppm) remained in the sample post-synthesis despite extensive drying *in vacuo*. Further handling and attempts to fully remove the toluene led to a small degree of decomposition. The toluene multiplets in the aromatic region mask three peaks expected in the compound but can be inferred from cross peaks detected in the COSY and ROESY experiments.

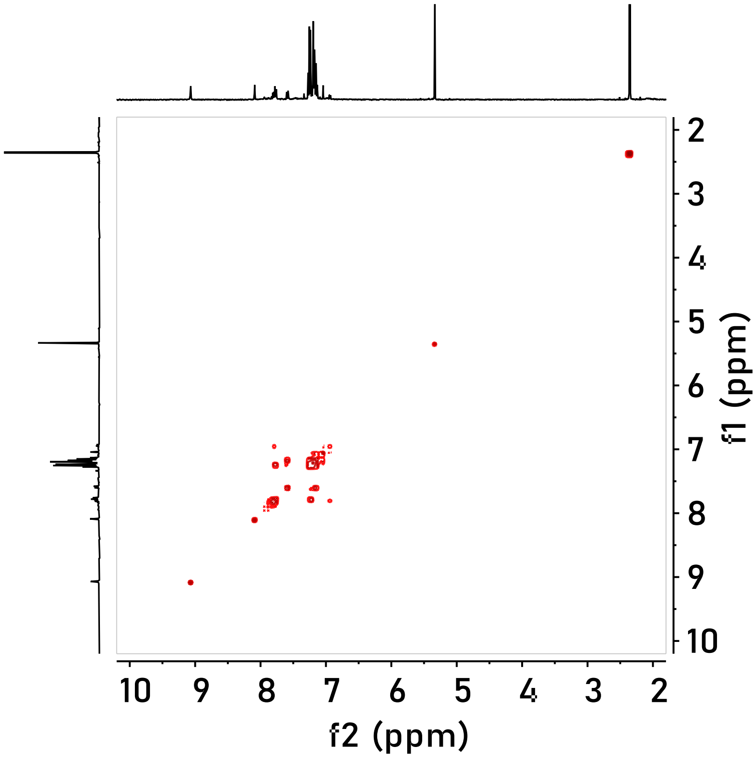

Figure A.48 Gradient COSY spectrum of NaDPP-Pent (400 MHz, CD_2Cl_2).

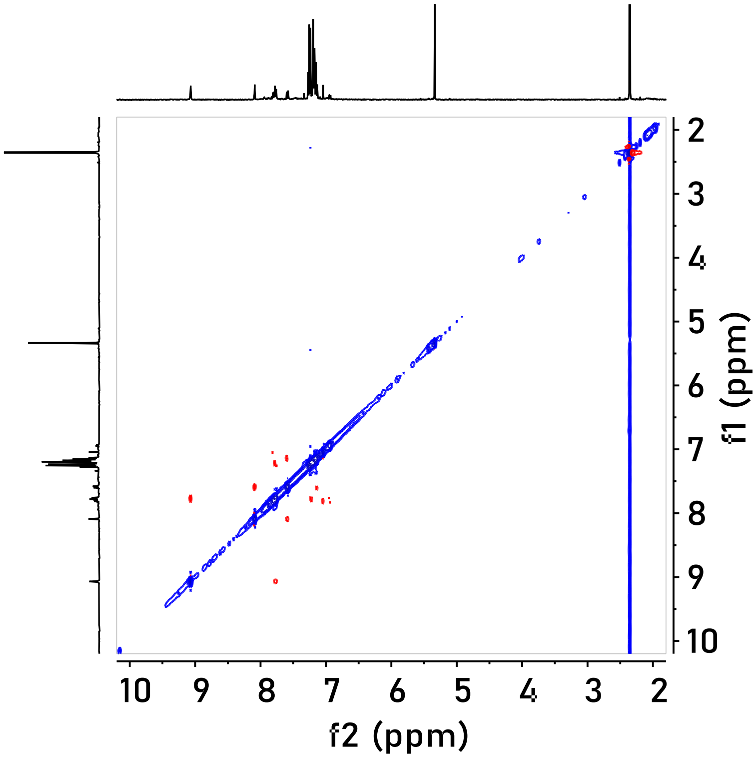

Figure A.49 2D ROESY spectrum of NaDPP-Pent (400 MHz, CD_2Cl_2).

XIV. $Li_2(DPP\text{-}Anth)_2$ Crystallographic Information

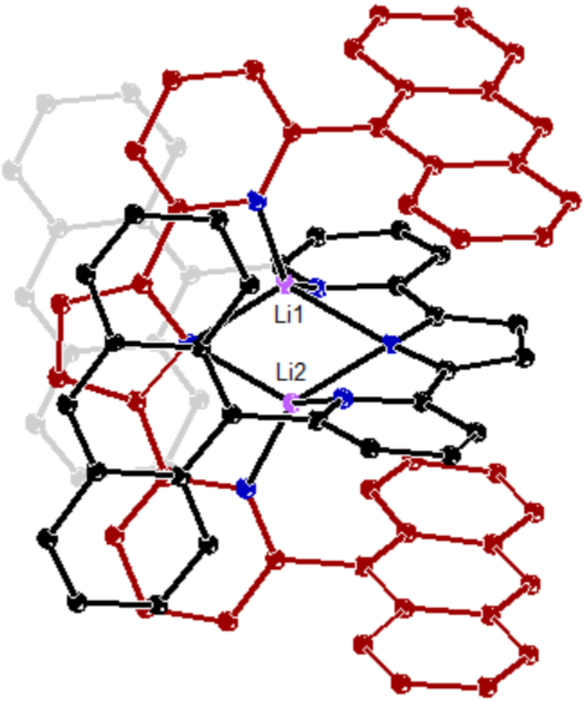

Figure A.50 X-ray crystal structure of $Li_2(DPP\text{-}Anth)_2$. The DPP-Anth ligand 1 and 2 are coded as black and red, respectively. Ellipsoids are drawn at the 50% probability level.

Table A.14 Crystal and refinement data for $Li_2(DPP\text{-}Anth)_2$

	$Li_2(DPP\text{-}Anth)_2$
CCDC	2031858
Empirical formula	$C_{84}H_{52}Li_2N_6$
Formula weight	1158.46
Temperature/K	100
Crystal System	Triclinic
Space group	P -1
a/Å	14.6365(8)
b/Å	15.1790(7)
c/Å	16.9748(11)
α/°	69.030(4)
β/°	68.970(5)
γ/°	70.059(4)
Volume/$Å^3$	3187.6
Z	2
$\rho_{calc}g/cm^3$	1.296
μ/mm^{-1}	1.331
F(000)	1297.0
Radiation	Cu Kα (λ = 1.54178)
2θ range for data collection	5.8 to 158.22
Index ranges	$-16 \leq h \leq 18$, $-18 \leq k \leq 14$, $-8 \leq l \leq 20$
Reflection collected	9802
Independent reflections	7982 [R_{int} = 0.0820, R_{sigma} = 0.1123]
Data/restraints/parameters	7982/0/856
Goodness-of-fit on F^2	1.081
Final R indexes [I>=2σ (I)]	R_1 = 0.0991, wR_2 = 0.2473
Final R indexes [all data]	R_1 = 0.1716, wR_2 = 0.2991
Largest diff. peak/hole/e $Å^{-3}$	1.16/-1.09

1. Lehnherr, D., McDonald, R. & Tykwinski, R. R. Exploring Electronically Polarized Pentacenes. *Org. Lett.* **10**, 4163–4166 (2008).
2. Seechurn, C. C. C. J., Sivakumar, V., Satoskar, D. & Colacot, T. J. Iridium-Catalyzed C–H Borylation of Heterocycles Using an Overlooked 1,10-Phenanthroline Ligand: Reinventing the Catalytic Activity by Understanding the Solvent-Assisted Neutral to Cationic Switch. *Organometallics* **33**, 3514–3522 (2014).
3. Snellenburg, J. J., Laptenok, S., Seger, R., Mullen, K. M. & Stokkum, I. H. M. van. Glotaran: A Java-Based Graphical User Interface for the R Package TIMP. *Journal of Statistical Software* **49**, 1–22 (2012).
4. Bensasson, R. & Land, E. J. Triplet-triplet extinction coefficients via energy transfer. *Trans. Faraday Soc.* **67**, 1904–1915 (1971).
5. Amand, B. & Bensasson, R. Determination of triplet quantum yields by laser flash absorption spectroscopy. *Chemical Physics Letters* **34**, 44–48 (1975).
6. Compton, R. H., Grattan, K. T. V. & Morrow, T. Extinction coefficients and quantum yields for triplet—triplet absorption using laser flash photolysis. *Journal of Photochemistry* **14**, 61–66 (1980).
7. Nielsen, B. R., Jørgensen, K. & Skibsted, L. H. Triplet—triplet extinction coefficients, rate constants of triplet decay and rate constant of anthracene triplet sensitization by laser flash photolysis of astaxanthin, β-carotene, canthaxanthin and zeaxanthin in deaerated toluene at 298 K. *Journal of Photochemistry and Photobiology A: Chemistry* **112**, 127–133 (1998).
8. Walker, B. J., Musser, A. J., Beljonne, D. & Friend, R. H. Singlet exciton fission in solution. *Nature Chemistry* **5**, 1019–1024 (2013).

9. Eaton, S. W. *et al.* Singlet Exciton Fission in Polycrystalline Thin Films of a Slip-Stacked Perylenediimide. *J. Am. Chem. Soc.* **135**, 14701–14712 (2013).
10. Zirzlmeier, J. *et al.* Singlet fission in pentacene dimers. *PNAS* **112**, 5325–5330 (2015).
11. Sanders, S. N. *et al.* Quantitative Intramolecular Singlet Fission in Bipentacenes. *J. Am. Chem. Soc.* **137**, 8965–8972 (2015).
12. Kumarasamy, E. *et al.* Tuning Singlet Fission in π-Bridge-π Chromophores. *J. Am. Chem. Soc.* **139**, 12488–12494 (2017).
13. Hetzer, C. *et al.* Chromophore Multiplication To Enable Exciton Delocalization and Triplet Diffusion Following Singlet Fission in Tetrameric Pentacene. *Angewandte Chemie International Edition* **58**, 15263–15267 (2019).
14. Korovina, N. V., Pompetti, N. F. & Johnson, J. C. Lessons from intramolecular singlet fission with covalently bound chromophores. *J. Chem. Phys.* **152**, 040904 (2020).